A 16-CHANNEL RECEIVE ARRAY INSERT FOR MAGNETIC RESONANCE IMAGING OF THE BREAST AT 7T

A Thesis

by

SAMANTHA BY

Submitted to the Office of Graduate and Professional Studies of
Texas A&M University
in partial fulfillment of the requirements for the degree of

MASTER OF SCIENCE

Chair of Committee,	Mary P. McDougall
Committee Members,	Steven M. Wright
	Melissa A. Grunlan
	Mark Lenox
Head of Department,	Gerard L. Coté

May 2014

Major Subject: Biomedical Engineering

ABSTRACT

Breast cancer is the second leading cause of cancer death among females in the United States. Magnetic resonance imaging (MRI) has emerged as a powerful tool for detecting and evaluating the disease, with notable advantages over other modalities, and the advent of ultra-high field strength scanners promises even more potential. In comparison to standard clinical MRI field strengths (1.5, 3.0 tesla), breast MRI at 7T provides increased signal-to-noise ratio (SNR) and spectral resolution. These benefits, however, are accompanied by significant challenges in hardware design, limiting the availability of commercial radiofrequency coils for 7T.

The primary objective of this work is to enable the study of breast cancer at 7T with the development of a 16-channel receive array coil. The use of array coils to receive is standard in clinical MRI, as it provides higher SNR over a field of view than a single coil. In this case, when combined with the increased sensitivity provided by the high field strength, this will enable the ability to acquire images with higher resolution than could be achieved at 3T or 1.5T in clinically standard scan times. This has the potential to improve the morphological characterization of tumors and their involvement in the surrounding tissues.

This thesis discusses the design and construction of a 16-channel receive array insert, characterization of its performance as an array, and comparison of the achievable SNR to a transmit-receive quadrature volume coil. With the 16-channel receive array insert, the results demonstrate a 6.5 times improvement in mean SNR and the ability to

accelerate up to a reduction factor of 9 with a mean *g*-factor of 1.3. Finally, we present initial in vivo images acquired with the array, demonstrating the utility of the array coil through higher resolution imaging than the current protocols at lower field strengths.

ACKNOWLEDGEMENTS

I am extremely grateful for the people I have been surrounded by during my first few years of my graduate school career.

First, I would like to thank my adviser, Dr. Mary McDougall. She is the most thoughtful, caring adviser I could ever ask for. With patience, she has always provided me with guidance and support, even when I didn't deserve it. I would also like to acknowledge Dr. Steven Wright, who has given me so much insight throughout this entire process. My other committee members, Dr. Melissa Grunlan and Dr. Mark Lenox, have also provided me with their invaluable time and input, and I thank you for that.

I would also like to acknowledge Drs. Craig Malloy, Ivan Dimitrov and Sergey Cheshkov at University of Texas Southwestern Medical Center for your patience on this project. All your long hours of testing that went into this work are very appreciated.

Thanks to all my lab mates, who have grown to become some of my best friends. You've made me look forward to going to the lab.

Finally, thanks to my family and friends, near and far, for your unconditional love and support that got me through this work.

TABLE OF CONTENTS

Page

ABSTRACT ii

ACKNOWLEDGEMENTS iv

TABLE OF CONTENTS v

LIST OF FIGURES vii

LIST OF TABLES xi

CHAPTER I INTRODUCTION 1

I.1 Motivation 1
I.2 Thesis Chapters and Organization 2

CHAPTER II BACKGROUND 4

II.1 The NMR Experiment 4
II.1.1 Polarization of Spins 4
II.1.2 Excitation and Reception of RF Signal 5
II.1.3 Gradients and k-space 8
II.2 High Field MRI 10
II.3 Parallel Imaging 11
II.3.1 Image Domain Based Parallel Imaging Methods 13

CHAPTER III CONSTRUCTION OF 16-CHANNEL BREAST RECEIVE ARRAY 15

III.1 Transmit Coil 15
III.2 Design and Construction of the 16-Channel Receive Array 17
III.2.1 Cable Management 23
III.3 Bench Measurements 28
III.3.1 Tuning 28
III.3.2 Quality Factor 31

CHAPTER IV PERFORMANCE EVALUATION OF 16-CHANNEL BREAST RECEIVE ARRAY 32

IV.1 Imaging Setup 32
IV.2 Noise Correlation Matrix 32
IV.3 SNR 35
IV.4 *g*-factor Evaluation 39

IV.5 Individual Field Patterns 42
IV.5.1 Testing of Receive Array Decoupling 44
IV.5.2 Testing for Incorrect Receive Array Cable Lengths 46
IV.5.3 Testing for Insufficient Transmit Coil Decoupling 48
IV.6 Conclusion 50

CHAPTER V IN VIVO IMAGING 51

V.1 Temperature Mapping for the 16-Channel Receive Array 51
V.1.1 IR Imaging 51
V.1.2 Calorimetry Readings 52
V.2 Imaging 54
V.2.1 Unaccelerated 54
V.2.2 Accelerated 55

CHAPTER VI CONCLUSIONS AND FUTURE WORK 59

REFERENCES 61

LIST OF FIGURES

Page

Figure 2.1: Polarization of spins. a) Spins are randomly oriented in free space such that it does not produce a net magnetic moment. b) When placed in an external magnetic field, an excess of spins will align in the direction of the polarizing field, resulting in a net magnetization. 5

Figure 2.2: Excitation and reception of RF signal. a) The magnetization vector starts in its equilibrium position, aligned with B_0. b) When a RF pulse is applied through a RF transmit coil, the magnetization vector tips into the transverse plane. The tip angle α is how much the magnetization vector tips into the transverse plane immediately after excitation. c) When the RF transmitter is turned off, the RF energy is retransmitted into the RF receive coil. d) After some time, the magnetization vector recovers back to its equilibrium position. 7

Figure 2.3: Gradient echo pulse sequence and its k-space trajectory. The slice select gradient is applied while an RF pulse is sent from the coil. G_{PE} is the phase encoding gradient, which moves the spins in *k*-space in the k_y-direction. G_{FE} is the frequency encoding gradient. To obtain an $N_P x N_F$ image, the echo is sampled N_F times during G_{FE}, and the entire pulse sequence is repeated N_p times. 9

Figure 3.1: Overview of transmit system. a) The 16-channel receive array was designed as an insert in a quadrature FCE transmit coil, which consists of a saddle pair (I.D. 152 mm) centered inside a Helmholtz pair (I.D. 160 mm). b) The use of FCE facilitates a simple method for detune. A pair of PIN diodes are placed at the common voltage point and present an open circuit to the transmit elements when biased. 16

Figure 3.2: Schematic of shell former for the array. The hemispherical shell had an inner diameter of 142 mm and a thickness of 3 mm to fit tightly inside the transmit coil. The polycarbonate shell was fabricated with a FDM rapid prototyping machine. 18

Figure 3.3: Overview of array geometry. a) Illustration of "soccer ball" geometry, where pentagons and hexagons are used to create overlapping circular coil elements. b) Layout of overlapped receive elements, highlighting each element's position and size (70 mm loops in blue, 59 mm loops in black). 19

Figure 3.4: Shaping coil elements onto a hemispherical shell. a) The PCB coil layout is designed and etched with an opening. The blue indicates the current paths, and the white segments serve as capacitor breaks. The black is the cutting outline. b) The coil element opening is pulled together, creating an element with six capacitive breaks. c) A cone cross section on the shell is shown, demonstrating how the coil element conforms to the surface of the hemispherical shell. 20

Figure 3.5: Circuit schematic of a single receive element including preamplifier chain. Each element is segmented by six breaks, with a passive and active detuning trap around the tune and match capacitors, respectively. 21

Figure 3.6: Photograph of detachable board. Due to the limited clearance inside the transmit volume coil, detachable boards including the active detuning trap, balun, and cable connection to 16-channel interface box were constructed and screwed onto their respective coils after inserting the receive array. 22

Figure 3.7: Photograph of one of the cable bundles. A cable trap tuned to 298 MHz was made around each bundle of cables. 23

Figure 3.8: Photographs of the completed 16-channel receive array. a) Custom made housing for the array includes side panels to prevent patient contact from circuitry. b) Close up of the 16-channel receive array inside the transmit coil. c) 16-channel receive array, with external boards connected, inside the FCE transmit coil, both housed in a custom-built former.....24

Figure 3.9: Schematic of receive element and necessary component values for voltage and power calculations. 25

Figure 3.10: Pulsed thermal impedance vs pulse width chart for M/A-COM 1072 diodes (73). 27

Figure 3.11: Measuring receive coil isolation. a) A schematic for the bench measurement is shown. The S_{21} of the receive coil is measured with a pair of decoupled probes. The isolation is defined as the difference in S_{21} when the coil is at 50 Ω and when it is biased with -5V (detune mode). b) Network analyzer trace demonstrating the isolation from a single receive element. 29

Figure 3.12: Bench testing setup for 16-channel receive array. The test setup includes a 16-channel fan out board that has the ability to detune all elements. 31

Figure 4.1: Noise correlation matrix. The noise correlation matrix demonstrates sufficient decoupling between elements (average: 5.7%, min: 1.36%, max: 22.61%). 34

Figure 4.2: Step-by-step details for calculating SNR map. As proposed by Kellman et al., two scans are required: a noise-only scan with RF amplifiers off and an additional scan with RF amplifiers on. The spatial SNR map is the resultant of the second scan divided by the standard deviation of a region in the noise-only image. 36

Figure 4.3. SNR maps of a homogenous canola oil phantom acquired with the volume coil (left) and the 16-channel receive array (right). Sagittal view is shown. Both maps were normalized to the maximum SNR from the 16-channel receive array (0 dB=1583 a.u. SNR). The 16-channel receive array demonstrates a mean SNR improvement of 6.5. 37

Figure 4.4: SNR profiles from the 16-channel receive array (blue) and the volume coil in T-R mode (red). The same column was extracted from each image for the comparison. 38

Figure 4.5: *g*-factor maps of a sagittal slice up to a nine-fold (F/H x L/R = 3 x 3) reduction factor. SENSE acceleration was applied in the left to right (L/R) and foot to head (F/H) directions using reduction factors of 1x, 2x, or 3x in each direction. With R = 9, the mean *g*-factor was 1.31 and the maximum *g*-factor was 2. 41

Figure 4.6: 3D volume renderings for individual elements in the array. 43

Figure 4.7: Results from low power scan. A gradient echo was used to assess whether traps were failing under power. Reconstruction of individual channels indicate that coupling was still present when the power was reduced. 44

Figure 4.8: B1 +field map (left) with relative line plots (right). The presence of the array did not deteriorate the homogeneity of the transmit field. 45

Figure 4.9: Results when receiving with only channel and other channels shorted. The results indicate that the receive array cable lengths don't seem to be the source of coupling. 46

Figure 4.10: Reconstruction of neighboring channels. With only channel 2 receiving, all other channels of the receiver box were terminated with a 50 Ω load. We expected to see noise in all other reconstructed channel

images, but the outline of the phantom is visible. 47

Figure 4.11: Results from scan testing for transmit detuning. The tests indicate that transmit detuning is at least partially detuning, but are likely the problem for the coupling patterns in the individual receive element field patterns. 49

Figure 5.1: Visible and thermal images of a breast canola oil phantom. Thermal images were obtained with a FLIR-17 camera before and after 30 minutes of heating. 53

Figure 5.2: 1x1x1 mm^3 image of a volunteer in all three planes (top left: sagittal, bottom left: coronal, bottom right: axial). 55

Figure 5.3: Breast images with increasing acceleration factors. SENSE was applied in the F/H direction for R=2 and R=3. For R=4, SENSE of 2 was applied in both L/R and F/H directions. A spatial resolution of 1 mm isotropic was achieved. 57

Figure 5.4: Ultra high resolution breast image with a SENSE of 3. Image acquired with a resolution of .5x.5x.5mm^3 58

LIST OF TABLES

Page

Table 3.1: Coil Element Sizing 19

Table 3.2: M/A-COM Diode Ratings 28

Table 3.3: Impedance and S_{11} of Individual Elements 30

Table 4.1: Reported Noise Correlation Matrices 34

Table 4.2: *g*-factors and Scan Times 42

Table 5.1: Calorimetry Readings for Temperature Mapping 54

CHAPTER I

INTRODUCTION

Magnetic resonance imaging (MRI) is a powerful, non-invasive imaging modality that provides excellent soft tissue contrast. The ability to visualize the body with such contrast has provided the opportunity to better characterize, treat, and understand a broad range of diseases. MR applications include, but are not limited to, brain, cardiac, vascular, breast, renal, and musculoskeletal imaging. The focus of this work is on breast MR.

I.1 Motivation

With an incidence rate of 1 in 8 women, breast cancer is the most common cancer in females worldwide (1,2). Less than 10% of breast cancer cases appear to have a genetic basis, however, bringing the need to study the etiology of the disease to the forefront in the effort to understand, prevent, and treat it. A method to increase sensitivity for in vivo characterization of the breast is highly significant.

Magnetic resonance imaging (MRI) has become a promising tool for breast imaging. Breast MRI at clinical field strengths (1.5T, 3T) has proven to be more sensitive than other conventional imaging modalities, such as x-ray mammography and ultrasound (3-11). In particular, MRI is especially advantageous in imaging dense breast tissue (12). The limits of breast MR, however, are still being pushed. Compared to clinical field strengths, the use of ultra-high fields inherently improves the sensitivity and spectral resolution. These benefits can be exploited for additional advantages, such

as improved spatial resolution and/or decreased scan times, offering new opportunities with respect to MR imaging and spectroscopy. It is anticipated that 7T MR will help understand the largely unknown etiology of breast cancer (13-24).

High fields, however, pose several technical challenges due to the increase in frequency of operation. This has limited the availability of hardware needed to enhance the capability of breast MR. As the field strength increases, the operational frequency increases and this produces short electromagnetic wavelengths in the human body (15,25). Consequently, it becomes more challenging to generate a homogenous B_1^+ transmit field within tissue while remaining within FDA regulations on the RF specific absorption rate (SAR) (26).

The use of array coils has been employed in most MRI applications. By simultaneously receiving signals from multiple small, independent receive coils, there is an increase in SNR, and this can also be traded for imaging time or higher resolution (27,28). This work describes the combination of the sensitivity gains from imaging at 7T with the gains from using an RF array coil in order to accomplish high resolution, both accelerated and unaccelerated, MR imaging of the breast.

I.2 Thesis Chapters and Organization

This main content of this thesis is divided into three specific aims:

Specific Aim 1: Design and construct a 16-channel receive array for 7T.

Specific Aim 2: Characterize the receive array insert with phantom imaging.

Specific Aim 3: Acquire in vivo images.

Following a brief background, the chapters of this thesis are organized by the specific aims. Chapter II will provide sufficient background on the MR experiment to understand this work. Chapter III will present the technical details of the design and construction of the array. The chapter addresses the decoupling methods of the array and also discusses the tuning process. Chapter IV will compare the 16-channel receive array insert with the currently available technology through phantom imaging. The SNR and *g*-factor served as the primary criteria for evaluation. Chapter V will demonstrate the utility of the array coil through high resolution in vivo imaging at 7T. Chapter VI reiterates the major contributions and significance of this work and presents potential future work.

CHAPTER II

BACKGROUND

The phenomenon of nuclear magnetic resonance (NMR) was first observed in 1946 independently by Felix Bloch and Edward Purcell (29,30). This led to the development of NMR spectroscopy, the study of the chemical structure of substances, and its significance was noted by awarding Bloch and Purcell the Nobel Prize of Physics in 1952. In 1973, Paul Lauterbur conceived the first MRI images through the use of spatially varying magnetic fields, also known as gradients (31). Subsequently, Peter Mansfield expanded on Lauterbur's work, focusing on methods for rapid acquisition of images (32). Since then, MRI has gradually evolved into a comprehensive tool used to gain anatomical and physiological information of the human body. In 2003, Lauterbur and Mansfield were recognized for their pioneering work in the early development of MRI with the Nobel Prize in Medicine.

II.1 The NMR Experiment

II.1.1 Polarization of Spins

MRI has the ability to image any atomic nuclei with an odd number of protons, because they possess an intrinsic angular momentum or "spin". The most imaged nucleus is that of hydrogen due to the abundance of water in the human body. Normally, the direction of these spins are randomly distributed (Fig. 2.1a), but when placed in an external magnetic field denoted B_0, the spins align parallel or antiparallel to the external magnetic field (Fig. 2.1b). A slight excess of spins aligns in the direction of the external

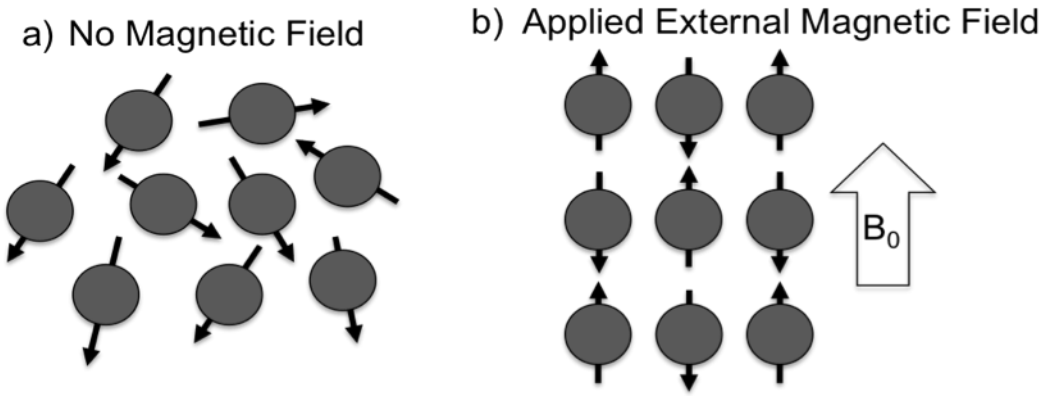

Figure 2.1: Polarization of spins. a) Spins are randomly oriented in free space such that it does not produce a net magnetic moment. b) When placed in an external magnetic field, an excess of spins will align in the direction of the polarizing field, resulting in a net magnetization.

field, resulting in a net alignment with the external field. This net magnetization is referred to as M_0 and is the source of the NMR signal. With MRI, the polarizing field is along the longitudinal direction, which corresponds to the z-axis. The transverse plane is denoted as the x-y plane perpendicular to the polarizing field.

The frequency at which the magnetization precesses about the axis of the main magnetic field B_0 is known as the Larmor frequency ω and is defined by:

$$\omega = \gamma B_0 \tag{2.1}$$

where γ is the gyromagnetic ratio for the nucleus of interest. For ^{1}H, the gyromagnetic ratio is 42.58 MHz/T.

II.1.2 Excitation and Reception of RF Signal

Fig. 2.2 depicts how the NMR signal is excited out of its equilibrium position (Fig. 2.2a) with B_0 and into the transverse plane such that a signal can be detected. An RF pulse is applied at the Larmor frequency through an RF transmitter, producing an

oscillating transverse field B_1 perpendicular to the static field. This consequently tips M_0 off the z-axis and into the transverse plane (Fig. 2.2b). The effect of the RF pulse is generally described by the tip angle α, the angle between the tipped magnetization and the longitudinal axis and is a function of the magnitude of the applied field and duration of the RF pulse.

When the RF transmitter is turned off, the magnetization continues to precess at the Larmor frequency in the transverse plane. By Faraday's law, the changing flux from the time-varying magnetization induces a voltage across an RF receive coil, which is oriented to detect the signal in the transverse plane (Fig. 2.2c). The magnetization vector then recovers back to equilibrium (Fig. 2.2d) according to relaxation processes.

T_1 relaxation is the longitudinal or spin-lattice time constant and refers to the return of the longitudinal magnetization M_z to equilibrium, M_0. The transverse relaxation component or the spin-spin relaxation is known as T_2. The complexity of the nuclear environment causes spins to precess at slightly different frequencies due to purely random spin-spin interactions, resulting in a dephasing of spins in the transverse plane and eventually losing the transverse magnetization. T_2^* refers to dephasing due to magnetic field inhomogeneities. The signal decay is primarily accounted by T_2 effects since T_1 is much longer than T_2.

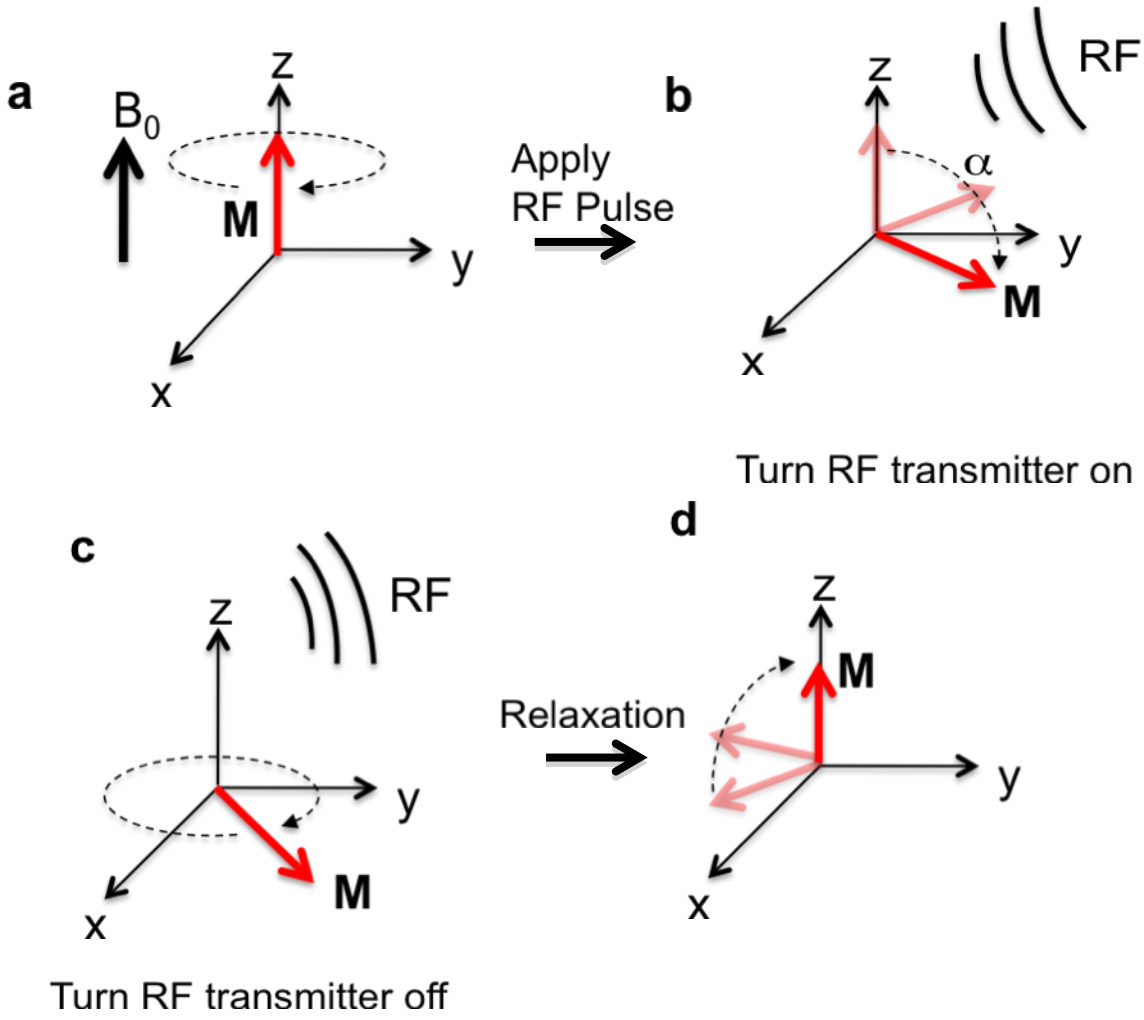

Figure 2.2: Excitation and reception of RF signal. a) The magnetization vector starts in its equilibrium position, aligned with B_0. b) When a RF pulse is applied through a RF transmit coil, the magnetization vector tips into the transverse plane. The tip angle α is how much the magnetization vector tips into the transverse plane immediately after excitation. c) When the RF transmitter is turned off, the RF energy is retransmitted into the RF receive coil. d) After some time, the magnetization vector recovers back to its equilibrium position.

II.1.3 Gradients and k-space

To spatially localize the signals and form an image, gradients (G_x, G_y, and G_z) are applied. Gradients are additional magnetic fields whose field strengths vary linearly with respect to position along x, y, and z. The separate gradients combine linearly to create a gradient field oriented in any direction that add to the main magnetic field:

$$B = (B_0 + G_x x + G_y y + G_z z)\hat{z} \tag{2.2}$$

Effectively, this allows the ability to map the signal. Since the variation in field strength corresponds to variation in the resonant frequency, the detected resonant frequency contributing to the resulting RF signal is now dependent on location.

The MR signals that are acquired as a result of the main magnetic field, RF coils, and gradients are stored in "k-space". A simplified gradient echo and its k-space trajectory are displayed in Fig. 2.3. An RF pulse is used to excite the spins and tip them 90 degrees. A slice select gradient G_{ss} is applied, typically in the z-direction and denoted as G_z in Eq. 2.2 above, at the same time as the RF excitation. This slice select gradient adds to the static field, and selectively excites a slice in the body, but localization of the spins in the other two directions is required before measuring the MR signal. A phase encoding gradient G_{PE} (typically in the y-direction, denoted as G_y above in Eq. 2.2) must be applied. Here, it is pulsed for a duration of T_P, causing all of the spins to rotate at a known angle. The phase encoding creates a phase shift in the signal derived from the sample that is a function of position in the direction perpendicular to the frequency encoding; this moves the magnetization in the $+k_y$-direction in k-space. Simultaneously a frequency encoding gradient, G_{FE} (typically in the x-direction, denoted as G_x above in

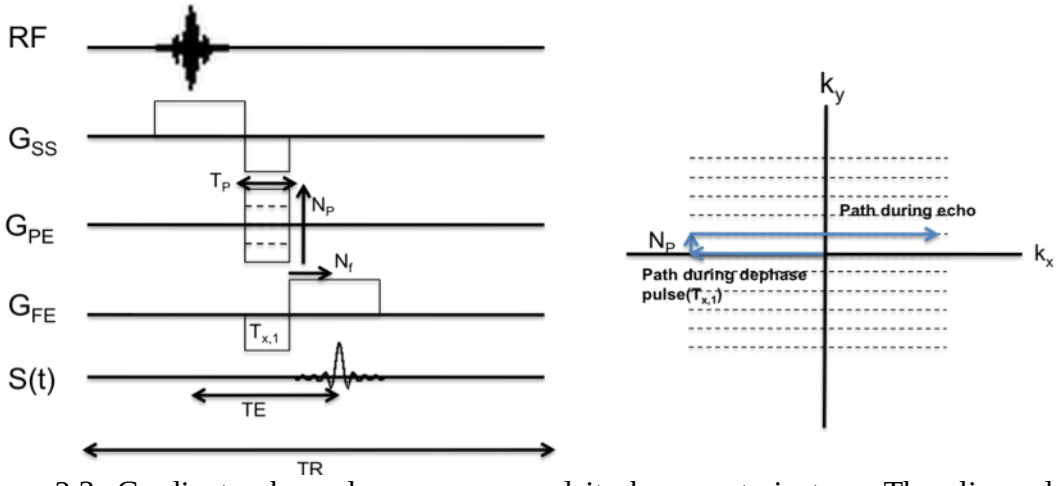

Figure 2.3: Gradient echo pulse sequence and its k-space trajectory. The slice select gradient is applied while an RF pulse is sent from the coil. G_{PE} is the phase encoding gradient, which moves the spins in *k*-space in the k_y-direction. G_{FE} is the frequency encoding gradient. To obtain an N_PxN_F image, the echo is sampled N_F times during G_{FE}, and the entire pulse sequence is repeated N_p times.

Eq. 2.2*)*, is applied to rapidly dephase all of the spins. The second gradient in the frequency encode direction moves the magnetization in the $+k_x$-direction and samples the signal so that the encoded signal is thus a function of the imparted phase and frequency. The echo time (TE) is the time from the start of the RF pulse to the center of the echo. The experiment is repeated N_p times, with the time between two consecutive RF pulses are known as the repetition time (TR).

The baseband MR signal during a gradient waveform is defined as:

$$S(t) = \iint_{slice} I(x,y) e^{j(\gamma G_x x t + \gamma G_y T_p y)} dx dy \tag{2.3}$$

where *I(x,y)* is the image to be formed. By defining *k*-space as

$$k_x = \gamma G_x t \qquad k_y = \gamma G_y T_p \tag{2.4}$$

the signal expression can be simplified to:

$$S(k_x, k_y) = \iint_{slice} I(x,y) e^{+jk_x x} e^{+jk_y y} dxdy \tag{2.5}$$

Eq. 2.5 makes it notably apparent that k-space is the Fourier transform of the image, and therefore an image can be obtained by applying the inverse Fourier transform to the raw data in k-space. These equations were derived from (33).

II.2 High Field MRI

The recent availability of commercially supported 7T research systems has enabled and fueled the interest in exploiting the benefits of high field imaging and spectroscopy to study disease, including breast cancer. The draw towards high fields stems from the increase in SNR: as the field strength increases, there is an increase in excess spins, thereby the availability of signal increases (34). The increase in SNR can be traded for other advantages; for example, SNR can be exchanged for higher spatial and/or temporal resolution, meaning increased coverage and shorter scan times (35).

Magnetic resonance spectroscopy (MRS) is also benefitted by higher field strengths. With increasing field strengths, there is a larger spectral separation between chemical species, resulting in increased spectral resolution (19,36). The application of high fields is especially useful, if not necessary, for low abundant non ^{1}H nuclei (17,37-39); the increased spectral resolution, along with the increase in SNR at high fields, consequently increases the sensitivity of metabolic profiling.

High field strengths can also provide different, perhaps better, contrast, than lower fields, but it is not quite as straightforward. As the field strength increases, there is a change in kinetics. The spin-lattice relaxation time, T_1, increases, while the spin-spin relaxation constants T_2 and T_2* tends to shorten (40,41). This implies that susceptibility effects increase with the strength of the magnetic field due to the increase in sensitivity for phase effects (42,43).

II.3 Parallel Imaging

As described earlier in II.1, it becomes evident that MRI acquisitions can be time-consuming with the need to repeat phase encoding steps in order to fully fill k-space. The introduction of phased array coils provide a key benefit over a single surface coil for MRI: by simultaneously receiving signals from multiple receive coils, there is an increase in SNR over a large field-of-view (FOV) (27). This increase in SNR can be traded to reduce scan time and ushered in the advent of parallel imaging.

With parallel imaging, differences in the receive sensitivities of the array elements are exploited to reconstruct an image with less data. Given the coil sensitivity maps, the origin of the signal is known and can be used to generate an image. Thus, by simultaneously acquiring data from multiple receive elements, the number of phase-encoding steps can be reduced, producing an aliased image with a reduced total acquisition time. This comes at the cost of reduced SNR by at least the square root of the reduction factor, *R*. In practice, SNR typically decreases more than this, and the additional losses are defined by the coil's geometry factor (*g*-factor) (44,45):

$$g = \frac{SNR_{full}}{SNR_{red} * \sqrt{R}} \tag{2.6}$$

The first theoretical proposal of using multiple coils as a means to reduce the number of phase encoding lines was introduced by Carlson in 1987 (46). In 1988, Hutchinson and Raff theoretically proposed the use of N equally spaced coils to fill an entire NxN image simultaneously, completely eliminating phase encoding (47). Realistically, however, this approach was hindered by hardware limitations.

In 1989, Kelton et al. introduced an image domain reconstruction method that utilized a more practical approach of "subencoding": a method that combined phase encoding with partial RF coil encoding and used a matrix inversion to unwrap an aliased image (48). Shortly following in 1993, Ra and Rim published a similar reconstruction method that would work where the reduction of phase encoding lines was less than or equal to the number of coils (49). The subencoding approach was refined in 1999 when Pruessmann et al. introduced a more robust formulation and implementation of these ideas and termed the method SENSitivity Encoding (SENSE) (44).

Other parallel imaging methods that have been proposed include, but are not limited to, SiMultaneous Acquisition of Spatial Harmonics (SMASH) (50), Partially parallel Imaging with Localized Sensitivities (PILS) (51), Sensitivity Profiles from an Array of Coils for Encoding and Reconstruction in Parallel (SPACE RIP) (52), and GeneRalized Autocalibrating Partially Parallel Acquisitions (GRAPPA) (53). Parallel imaging techniques can be reconstructed either in the k-space domain or in the image domain. SENSE was implemented as the parallel imaging method for the work in this

thesis, and thus a more thorough description of image domain methods will be provided. Details on k-space and hybrid domain methods can be found in references (50,53-55).

II.3.1 Image Domain Based Parallel Imaging Methods

In an image-based method, coil sensitivities are used to "unfold" the resulting aliased image from undersampling *k*-space. A two-coil array will be used as an example, as discussed in (54). With a factor of two acceleration, an aliased image will be produced, overlapping pixels *a* and *b*. Each pixel must be weighted by the coil sensitivity at that same pixel before adding the two pixels together. Therefore, the signal received at coil 1 from a single pixel in the aliased image (A_1) is calculated as:

$$A_1 = C_1(a)I(a) + C_1(b)I(b) \tag{2.7}$$

where C_1 is the sensitivity of coil 1, and I is the fully encoded image information. With two unknowns, a second equation must be derived using the other coil with different sensitivity C_2. A pixel in the folded image of coil 2 (A_2) can be written as:

$$A_2 = C_2(a)I(a) + C_2(b)I(b) \tag{2.8}$$

Rearranging in matrix form, we are provided with two equations to solve for two unknowns:

$$\begin{bmatrix} A_1 \\ A_2 \end{bmatrix} = \begin{bmatrix} C_1(a) & C_1(b) \\ C_2(a) & C_2(b) \end{bmatrix} \begin{bmatrix} I(a) \\ I(b) \end{bmatrix} \text{ or } A = C * I \tag{2.9}$$

By inverting the coil sensitivity and multiplying it with the aliased signals, the image can be "unwrapped" to synthesize the unknown pixel intensities and produce an unaliased image:

$$\begin{bmatrix} I(a) \\ I(b) \end{bmatrix} = \begin{bmatrix} C_1(a) & C_1(b) \\ C_2(a) & C_2(b) \end{bmatrix}^{-1} \begin{bmatrix} A_1 \\ A_2 \end{bmatrix} \text{ or } I = C^{-1} * A \tag{2.10}$$

This chapter has provided background on MRI, high fields and parallel imaging. In the next chapter, we discuss the construction of an array coil for 7T.

CHAPTER III

CONSTRUCTION OF 16-CHANNEL BREAST RECEIVE ARRAY

MRI has emerged as a power tool for breast imaging, owing to its ability to provide high sensitivity and resolution (8-11). At low field strengths, these benefits have been limited by the achievable signal-to-noise ratio (SNR) (13,56), irrespective of hardware improvements (57-59), thus motivating recent interest in breast imaging and spectroscopy at 7T (13-19).

As with much of the 7T research at this time, a large portion of the work in breast imaging has been focused on optimizing the radiofrequency (RF) coil design (16,24,60-67). Unilateral and bilateral breast receive array coils with up to 30 elements have been presented (20-23). We have previously reported the advantages of transmitting with "forced current excitation" (FCE) in the design of a highly homogenous quadrature volume breast coil for 7T (61,62). This chapter first provides an overview of the transmit coil the array was designed for, and then provides details for the design and construction of the 16-channel receive insert.

III.1 Transmit Coil

All hardware was designed and tested for use on a whole-body 7T scanner (Achieva, Philips Medical Systems, Cleveland, OH). The transmit coil was a previously reported Helmholtz-saddle configuration for highly homogenous quadrature excitation of the pendant breast using forced current excitation (FCE) (61). In this design, connecting the two elements of each Helmholtz or saddle pair to a common voltage point (CVP) with

quarter wavelengths of transmission line forced equal currents to be delivered to the top and bottom loops of the Helmholtz pair and to the two elements in the saddle pair. The resulting transmit field was highly homogenous, despite the asymmetric loading presented by the thorax when imaging the pendant breast and, more significantly, in the presence of the asymmetric loading presented by the array insert. A rendering of the volume coil with the receive array insert and diagram of the FCE implementation is shown in Fig. 3.1. The Helmholtz loops had an inner diameter of 160 mm and the saddle elements were constructed on a cylindrical tube with an inner diameter of 152 mm and centered inside of the Helmholtz pair. The saddle elements were segmented by twelve

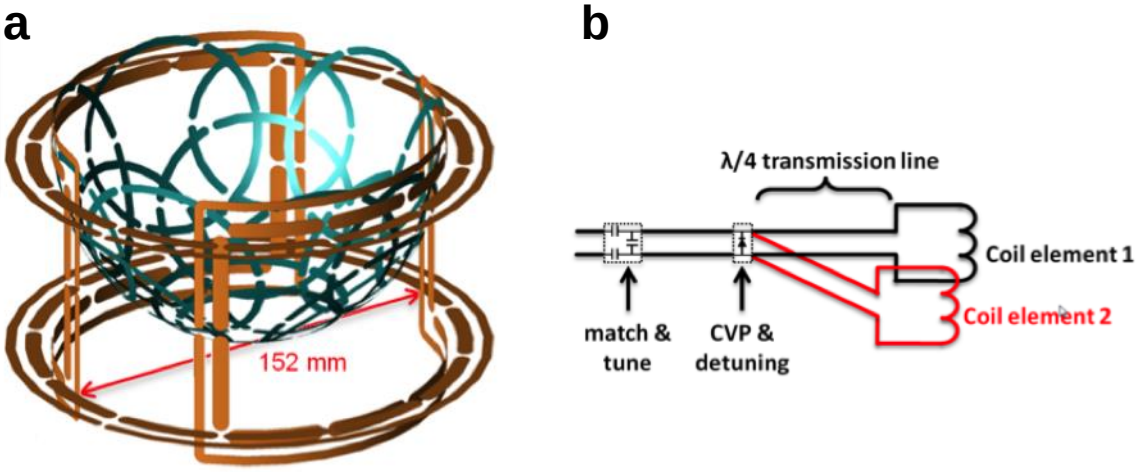

Figure 3.1: Overview of transmit system. a) The 16-channel receive array was designed as an insert in a quadrature FCE transmit coil, which consists of a saddle pair (I.D. 152 mm) centered inside a Helmholtz pair (I.D. 160 mm). b) The use of FCE facilitates a simple method for detune. A pair of PIN diodes are placed at the common voltage point and present an open circuit to the transmit elements when biased.

breaks and the Helmholtz elements with twenty breaks.

The FCE configuration enabled straightforward detuning of the transmit coil during receive. As illustrated in Fig. 3.1b, a shunt PIN diode (UM9415, Microsemi) was placed on the CVP such that when forward-biased during receive, the quarter wavelength lines presented open circuits to the transmit coil elements. As an additional advantage, this approach created separation between the DC control lines and the field-of-view.

III.2 Design and Construction of the 16-Channel Receive Array

The 16-channel receive array was constructed on a polycarbonate hemispherical shell fabricated with a fusion deposition modeling (FDM) rapid prototyping machine. All prototyped parts were drawn in Solidworks. The shell had an inner diameter of 142 mm and a thickness of 3 mm (Fig 3.2).

Element size and placement on the shell were determined by arranging pentagonal and hexagonal tiles in the "soccer ball geometry" presented by Wiggins et al. (68). As illustrated in Fig. 3.3a, a circular coil is formed around the vertices of the tiles, where the center of the tiles corresponds to the center of the circular coils, creating an overlap between elements. Since a pentagon covers a smaller area than a hexagon, this results in coils with two different inner diameters. The resulting layout consisted of ten coils with an inner diameter of 70 mm and six coils with an inner diameter of 59 mm in an overlapping 1-6-9 coil arrangement over three tiers, as shown in Fig. 3.3b. Coils are numbered starting with 1 at the apex and increase at each layer clockwise. Table 3.1

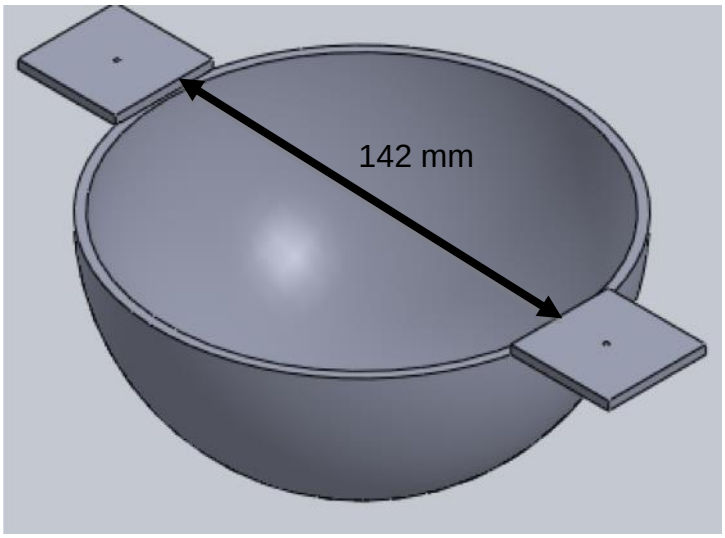

Figure 3.2: Schematic of shell former for the array. The hemispherical shell had an inner diameter of 142 mm and a thickness of 3 mm to fit tightly inside the transmit coil. The polycarbonate shell was fabricated with a FDM rapid prototyping machine.

below indicates the sizes of each individual coil element. Elements were fabricated from 0.2 mm thick copper-clad FR-4 printed circuit board (PCB). Each loop was etched as a "C"-shaped gore, with an opening that when pulled together resulted in a loop conformed to the surface of the hemispherical shell (Fig. 3.4) (57).

Each element had six breaks, utilized as shown in Fig 3.5. Fixed capacitors (9.1 pF and 11 pF, 1111C series, Passive Plus) were placed across four breaks, and a variable tuning capacitor (46MN series, Passive Plus) was placed across the break opposite the feed. Using the standard single-active-trap approach that is used at lower fields (69-71) did not adequately decouple the array during transmit, manifesting as inhomogeneites around the perimeter of the image close to the elements. Therefore, fast switching back-to-back diodes (UM9989B, Microsemi) and a variable inductor (164 series, Coilcraft) in

parallel with the tuning capacitor formed a passive trap to further increase isolation of the element during transmit (when the diodes are forward biased) (72).

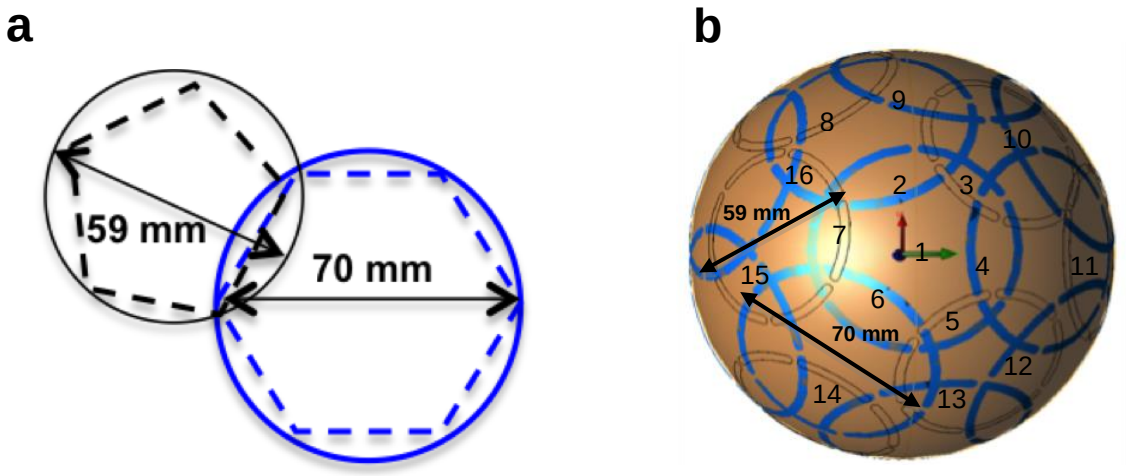

Figure 3.3: Overview of array geometry. a) Illustration of "soccer ball" geometry, where pentagons and hexagons are used to create overlapping circular coil elements. b) Layout of overlapped receive elements, highlighting each element's position and size (70 mm loops in blue, 59 mm loops in black).

Table 3.1: Coil Element Sizing

	59 mm loops	**70 mm loops**
Coil number	3,5,7,8,11, 14	1, 2, 4, 6, 9, 10, 12, 13, 15, 16

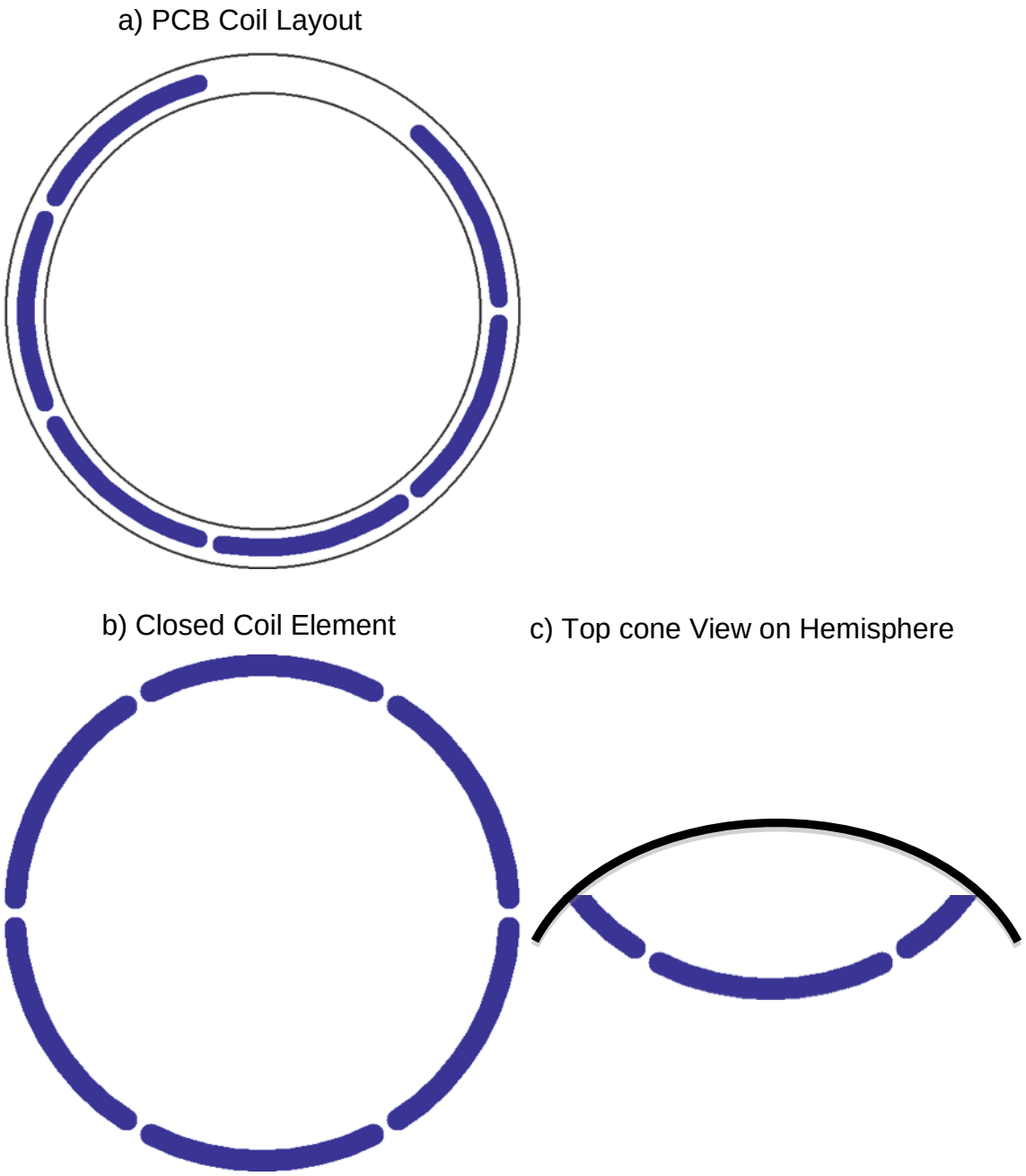

Figure 3.4: Shaping coil elements onto a hemispherical shell. a) The PCB coil layout is designed and etched with an opening. The blue indicates the current paths, and the white segments serve as capacitor breaks. The black is the cutting outline. b) The coil element opening is pulled together, creating an element with six capacitive breaks. c) A cone cross section on the shell is shown, demonstrating how the coil element conforms to the surface of the hemispherical shell.

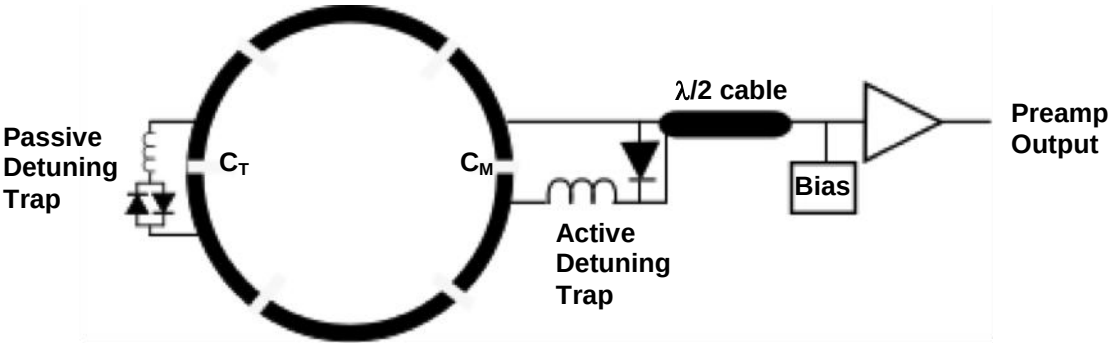

Figure 3.5: Circuit schematic of a single receive element including preamplifier chain. Each element is segmented by six breaks, with a passive and active detuning trap around the tune and match capacitors, respectively.

Given the limited clearance and fit inside the transmit coil, required circuits at the element feed points were located on detachable circuit boards and connected after inserting the array. These boards contained the active trap configuration (described further below), a balun, and a "hard-wired" half-wavelength coaxial cable (G_02232_D, Huber+Suhner) connecting to the isolating preamplifiers and bias control housed in the Philips 16-channel receiver interface box. An SMA plug connected to the feed point of the element allowed for direct connection to an end-launch SMA receptacle on the detachable board. A labeled photograph of one of the 16 boards is shown in Fig. 3.6. The balun was constructed from a user-tunable prefabricated inductor can (3T-CC-3T, Correct Coil). The active trap consisted of a PIN diode (MA4P7470F-1072, Macom), a variable inductor (164 series, Coilcraft), and a fixed match capacitor (13-33 pF, 1111C series, Passive Plus). This trap formed a parallel resonant circuit when the diode was forward biased via the 16-channel receiver interface box.

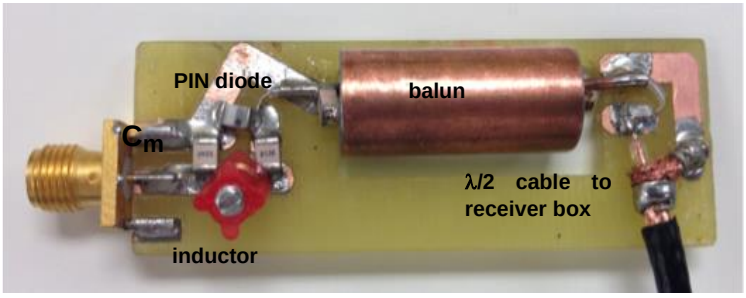

Figure 3.6: Photograph of detachable board. Due to the limited clearance inside the transmit volume coil, detachable boards including the active detuning trap, balun, and cable connection to 16-channel interface box were constructed and screwed onto their respective coils after inserting the receive array.

A half-wavelength of electrical length must separate the receive coil's detuning trap and the preamplifier in the receiver box. This ensures that a low input impedance at the preamplifier is present across the detuning trap at the Larmor frequency, consequently introducing a high impedance to the loop coil. To account for the unknown electrical length in the Philips receiver box, the correct cable length had to be determined.

As shown previously in Fig. 3.6, a coaxial cable connects the receiver box to the receive board, with a balun in between the coaxial cable and detuning trap. On a single receive element, a connector was soldered across the feed point of the detuning trap after the balun (where the transmission line ends). Following a port extension calibration on the network analyzer, we used a line stretcher to connect the receive element's board (before the balun) to one port of the Philips receiver box. The line stretcher enabled us to vary the electrical length, and thus, the "cable length" was easily modified. Using the Smith chart mode on the network analyzer, the length of the line stretcher was varied

until a short, or low input impedance, was observed at the detuning trap. The length of the line stretcher was recorded and all the receive cables were trimmed according to this measurement (~119 cm).

III.2.1 Cable Management

The 16 cables were bundled in groups of five or six and cable traps were created for each bundle to control any induced currents on the cable shields. A shielded, expandable copper mesh (5537K27, McMaster Carr) was wrapped around the cable bundles. The inductance of the bundles was used with a parallel capacitor to tune the cable trap to 298 MHz, as highlighted in Fig. 3.7 (71). The bundles were routed through channels that allowed for either left or right side breast imaging. Side panels were fabricated to prevent the patient from contacting any of the circuitry. Photographs of the array with the external boards attached inside the transmit coil is shown in Fig. 3.8.

Figure 3.7: Photograph of one of the cable bundles. A cable trap tuned to 298 MHz was made around each bundle of cables.

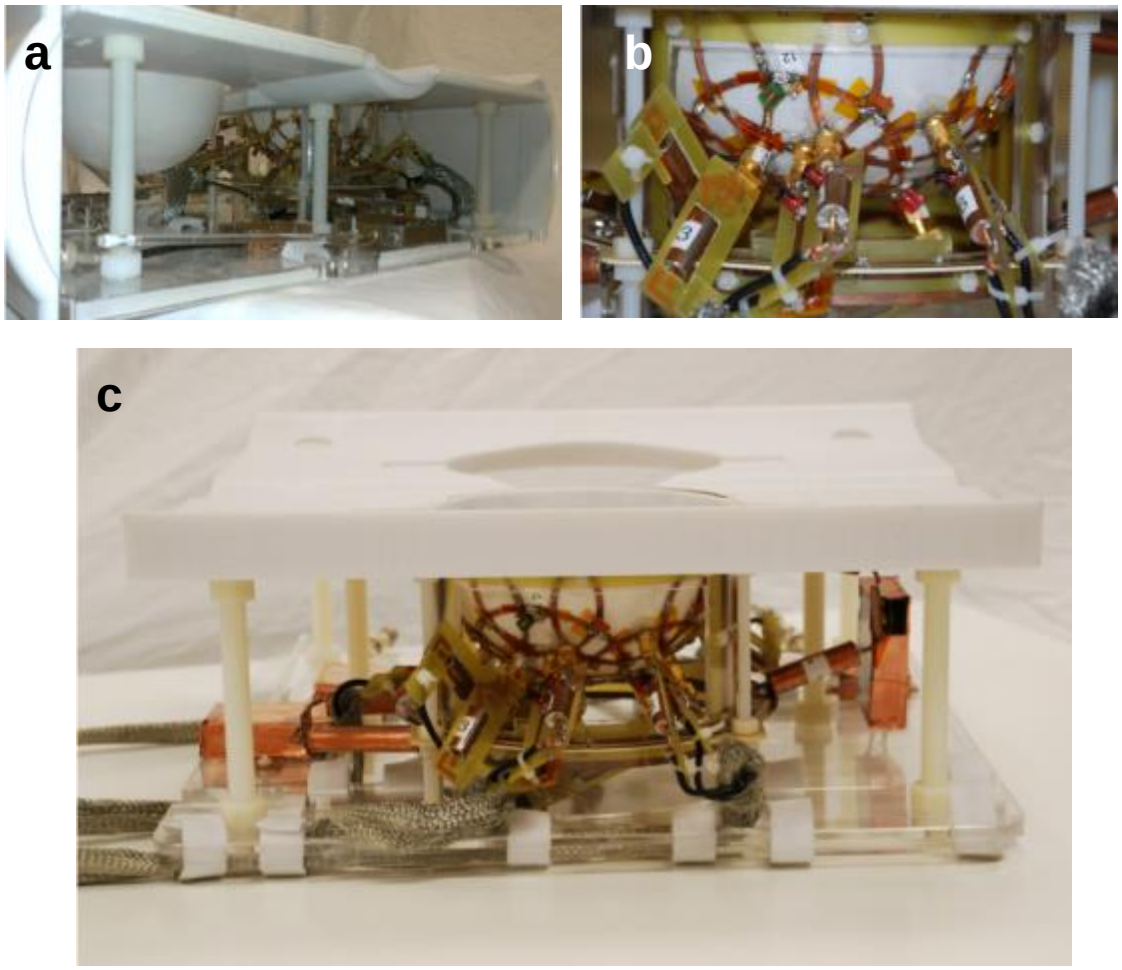

Figure 3.8: Photographs of the completed 16-channel receive array. a) Custom made housing for the array includes side panels to prevent patient contact from circuitry. b) Close up of the 16-channel receive array inside the transmit coil. c) 16-channel receive array, with external boards connected, inside the FCE transmit coil, both housed in a custom-built former.

III.2.2 Components

At high fields, voltage ratings for components must be carefully assessed, even for receive arrays. Erring on the safe side, capacitors were chosen to have a DC withstanding voltage of 1500 V when possible. The tight fit of the array insert inside the

transmit coil required a physically small variable tuning capacitor, and those had a DC withstanding voltage of 1100 V.

Originally, the traps used the Microsemi 9401 diodes, which are rated for 50 V of reverse voltage when the diode is off. Diode failure, however, was observed on the bench when the array was reexamined after imaging. This led us to calculate the maximum voltage being induced across the diode and the amount of power the diode is dissipating in our experiments. We then used our experimental calculations to replace the diode with one whose rated specifications are better suited.

This calculation was a "worst-case" analysis, and thus we assumed a 7 cm receive coil fully coupled to the B_1 transmit of 20 μT (i.e. a receive element that is coplanar to the saddle coil). A schematic of the coil and its values are shown in Fig 3.9 below. The capacitance and resistance of the diodes are an average approximation using the curves provided by various specification sheets for the diodes.

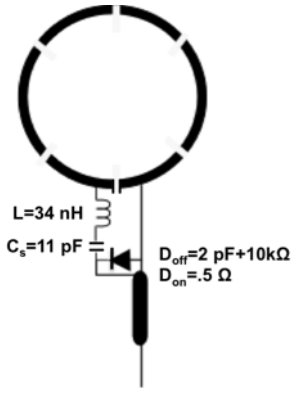

Figure 3.9: Schematic of receive element and necessary component values for voltage and power calculations.

With these assumptions, the following impedance calculations were made:

$$Z_{CS} = \frac{1}{j\omega C} = -48.6j\Omega \tag{3.1}$$

$$Z_{d,off} = 10{,}000 + \frac{1}{j\omega C} = 10k - 267j\Omega \tag{3.2}$$

$$Z_{d,on} = .5\Omega \tag{3.3}$$

$$Z_{CS} + Z_L + Z_{d,off} = Z_{series,off} = 10k - 252j\Omega \tag{3.4}$$

$$Z_{CS} + Z_L + Z_{d,on} = Z_{series,on} = .5 + 15.1j\Omega \tag{3.5}$$

where *CS* is the capacitor placed in series to the inductor, *L* is the inductor, and *D* is the diode. With the impedance calculations, the current is calculated for when the diode is on and when it is off:

$$emf = j\omega BA = j(2\pi * 298\ MHz) * (20\ \mu T) * \pi(.035\ m)^2 = \ 144j\ (V) \tag{3.6}$$

$$I_{off} = \frac{emf}{Z_{series,off}} = -.0005 + .0144j\ (Amps) \tag{3.7}$$

$$I_{on} = \frac{emf}{Z_{series,on}} = 9.5 + .315j(Amps) \tag{3.8}$$

Consequently, for our experiments, using the respective impedances and current, the expected voltage across the diode when it is off is calculated as 144 V and the maximum power that the diode is dissipating when it is on is 45.4 W.

Next, we estimated how much power different diodes could withstand. The power dissipated by the diode is dependent on the resistance of the diode. To estimate the maximum power dissipation of a diode possible before failure, we referred to the "Diode Resistance vs Pulse Width" curve provided in the M/A-COM specification

sheets and shown in Fig. 3.10 below for convenience. The maximum diode junction temperature is always 175°C, indicating that if the diode junction temperature were to exceed 175°C during operation, the diode would be subject to failure (73).

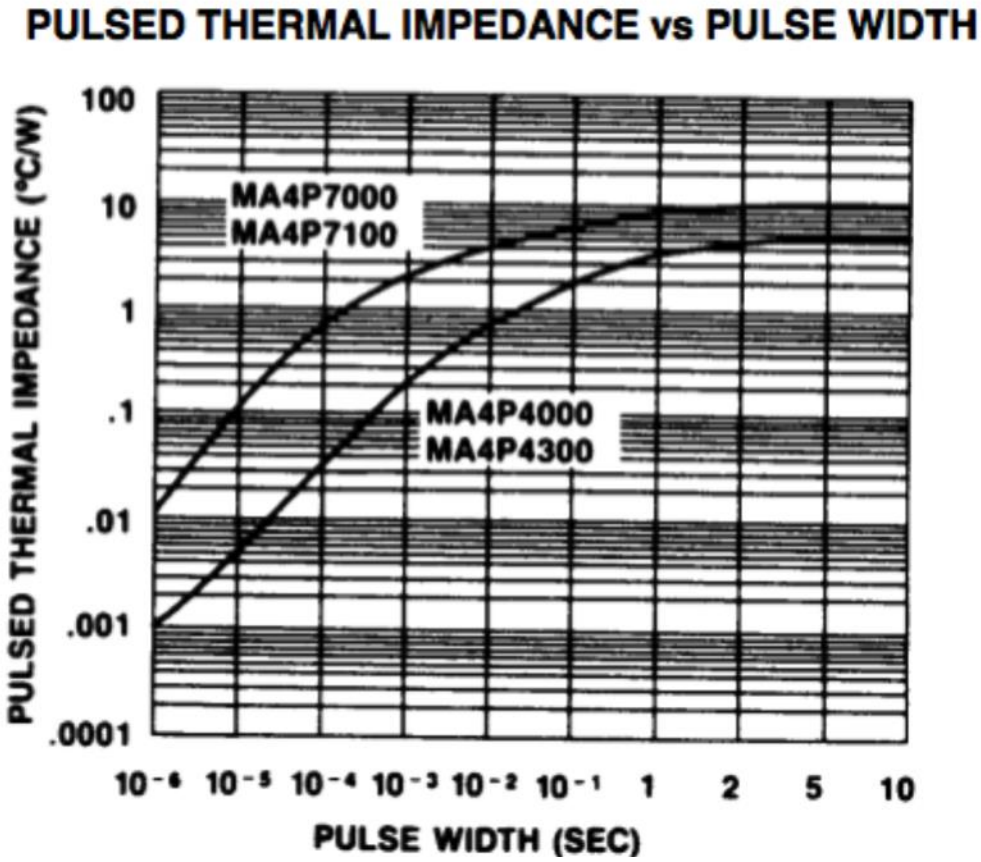

Figure 3.10: Pulsed thermal impedance vs pulse width curve for M/A-COM 1072 diode (73).

The maximum output power of the Philips transmitter can be as high as 4 kW; the maximum pulse length is 10 ms, but because the pulses are shaped, it was assumed that the peak power level occurred at 30% of the maximum total pulse length. For the 7x700 series, as shown in Fig. 3.10 above, the PIN diode thermal resistance for the

7x700 series is rated as 3°C/W at 3 ms. Thus, the maximum power dissipation rating for the M/A-COM diodes is approximately 50W. This satisfies our experiments' "worst-case" power dissipation calculation of 45 W when the diode is on. Approximately, given our pulse length, the power dissipation rating for the Microsemi 9401 diodes is only 44 W. This does not adequately satisfy the calculated power dissipation of 45.4 W in the worst case scenario, and potentially indicates why they failed under power. Thus, we chose the M/A-COM 1072 diodes for our traps, whose ratings are shown in Table 3.2 below. In addition, the elements were matched with fixed capacitors with higher power ratings than the 100 V variable capacitors (9350 Series, Johanson Manufacturing) previously used.

Table 3.2: M/A-COM Diode Ratings

	Maximum Voltage	Capacitance	Resistance
M/A-COM MA4P7470F-1072	800 V	.7 pF	.8 Ω

III.3 Bench Measurements

III.3.1 Tuning

Since the external board included the match capacitor, disconnecting the board open-circuited the corresponding receive element; thus, removing all but one board created an isolated setting for tuning a single element. Tuning the array was an iterative process. Inside the detuned transmit coil, each element was first tuned with no other

boards connected. Once an individual element was matched and tuned to 50 Ω, a capacitor was removed from the coil in order to tune the active trap on a non-resonant structure. With the diode forward biased with an external 100 mA source, an inductor probe was used to detect the resonant frequency of the trap and the variable inductor was adjusted until the trap was tuned to 298 MHz. The isolation provided by the trap for each coil element was measured as the change in the S_{12} measurement between two decoupled, shielded probes when the PIN diode was unbiased and biased. Isolation was greater than 20 dB in all cases (Fig. 3.11). To ease the tuning process, variable capacitors

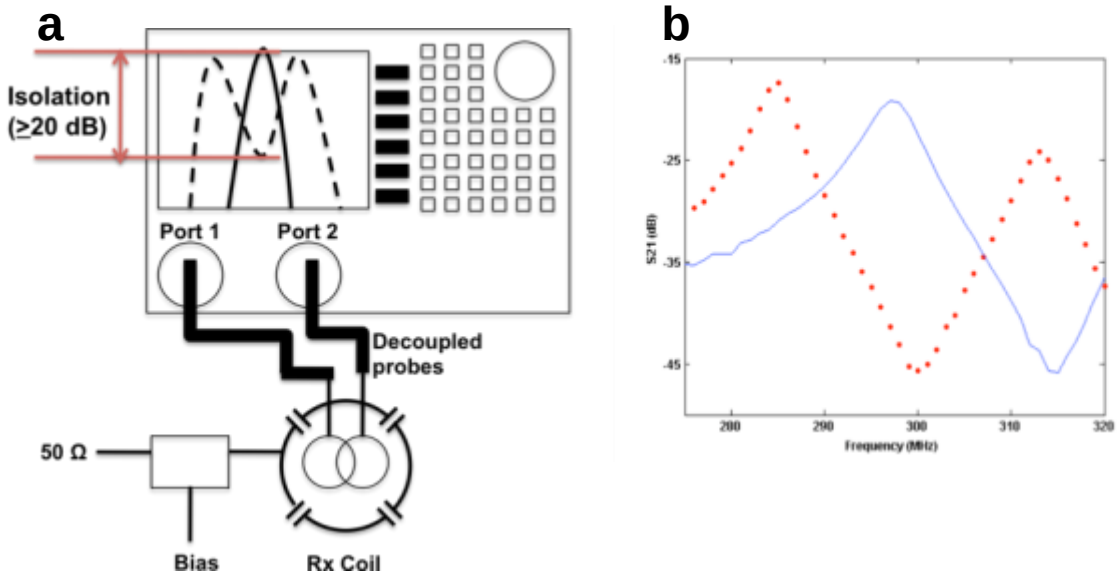

Figure 3.11: Measuring receive coil isolation. a) A schematic for the bench measurement is shown. The S_{21} of the receive coil is measured with a pair of decoupled probes. The isolation is defined as the difference in S_{21} when the coil is at 50 Ω and when it is biased with -5V (detune mode). b) Network analyzer trace demonstrating the isolation from a single receive element.

were used for the match capacitor, but replaced with a fixed value once tuning was complete. The impedances and S_{11} of each coil are listed in Table 3.3.

Table 3.3: Impedance and S_{11} of Individual Elements

Coil Number	Z (Ω)	S_{11}
1	45.4-8.3j	-20 dB
2	48+20j	-15 dB
3	55-5j	-23 dB
4	47+2j	-29 dB
5	41-3j	-20 dB
6	58-5j	-20 dB
7	48+16j	-16 dB
8	55-3j	-24 dB
9	43+6j	-20 dB
10	52-13.4j	-18 dB
11	38-11 j	-15 dB
12	59-3.2j	-22 dB
13	50+.8j	-40 dB
14	50-2.2 j	-30 dB
15	53+.2j	-31 dB
16	58+8j	-19 dB

Once all elements and the traps were individually tuned, the boards were attached to the array elements. The elements were hooked up to a 16-channel "fan out board", which provided -5V from a detuning box to mimic the receiver box during transmit (Fig 3.12). During receive, the receiver box provides +12V. With all of the other elements biased, each element's tuning had to be tweaked due to some shielding effects from the receive array's external boards.

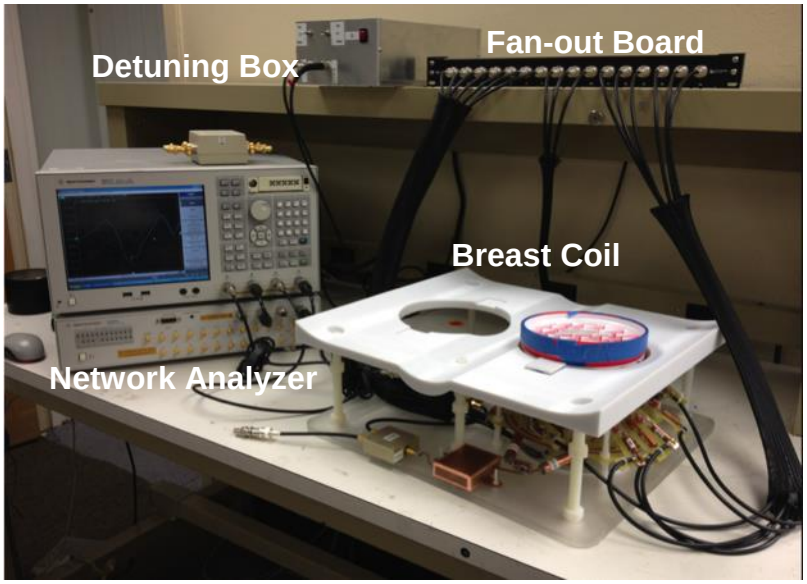

Figure 3.12: Bench testing setup for 16-channel receive array. The test setup includes a 16-channel fan out board that has the ability to detune all elements.

III.3.2 Quality Factor

The quality factor (Q) is an indicator of resistive losses in the coil and SNR. Q is defined as:

$$Q = \frac{\omega L}{R} \tag{3.9}$$

where L and R are the inductance and resistance of the coil respectively. On the bench, one method for straightforwardly measuring Q is to use the -7 dB width around the minimum of the S_{11} response (74). The completed 58.5 mm loops had a Q of 48, and the 70 mm loops had a Q of 40. It was observed that the presence of the passive trap decreased the Q almost by a factor of 2. This is mainly due to the addition of another inductor, and will need to be addressed in future modifications of the coil. For both coil sizes, however, the $Q_{UL} >> Q_{L,}$ indicating the elements are still sample noise dominant.

CHAPTER IV

PERFORMANCE EVALUATION OF 16-CHANNEL BREAST RECEIVE ARRAY

This chapter describes the evaluation of the performance of the 16-channel receive array. The metrics used were a comparison of signal-to-noise ratio (SNR) to a quadrature volume coil, noise correlation matrix measurement, and *g*-factor calculation.

IV.1 Imaging Setup

All hardware was designed and tested for use on a whole-body 7T scanner (Achieva, Philips Medical Systems, Cleveland, OH). The array first was tested using a uniform phantom for SNR calculations. The former of the phantom was a rapid-prototyped hemispherical shell with an inner diameter of 135 mm, sized such that it would tightly fit inside the array to maximize the filling factor of the array. The phantom was filled with canola oil to mimic the loading properties of the breast (75). Unless otherwise noted, a 3D T_1 High-Res Isotropic Volume Excitation (THRIVE) sequence was used for imaging. The comparison coil to evaluate the performance of the array was the FCE quadrature transmit volume coil operating in transmit-receive (T-R) mode without the array in place.

IV.2 Noise Correlation Matrix

The noise correlation matrix is an important measure when assessing receive array coil design, as it dictates the array's ability to increase SNR or decrease acquisition times (76). The noise correlation matrix is generated by obtaining a "noise-only" scan with the RF amplifiers turned off. To properly generate a noise-only scan, certain Philips

software protocol had to be followed: the CLEAR parameter must be set to ‘no’ and SENSE must be set to ‘yes’ with the reduction factor set to 1.0. Without SENSE=’yes’, the CLEAR parameter will not be visible and it will not be possible to obtain a uniform noise image. Each channel was individually reconstructed from the noise-only scan and using this data, the noise correlation matrix was generated in MATLAB by using the built-in command for calculating matrix correlation coefficients.

The noise correlation matrix for the array is displayed in Fig. 4.1 below. The mean noise correlation between elements is 5.7% (min: 1.36%, max: 22.61%), indicating a high degree of isolation between elements. Table 4.1 lists a number of reported mean and maximum noise correlation values for different breast coils as a measure of comparison. As shown, to our knowledge, the only reported noise correlation matrix for a 7T breast coil is for a 30-channel unilateral breast coil (20). Noise correlation matrices for two different breast coils at 3T have been reported in (57); these reported values are for bilateral coils, and as such, the mean and maximum values would actually increase if looking at only the unilateral case. In comparison to other published breast arrays, our noise correlation matrix indicates sufficient decoupling between elements in our custom 16-channel array.

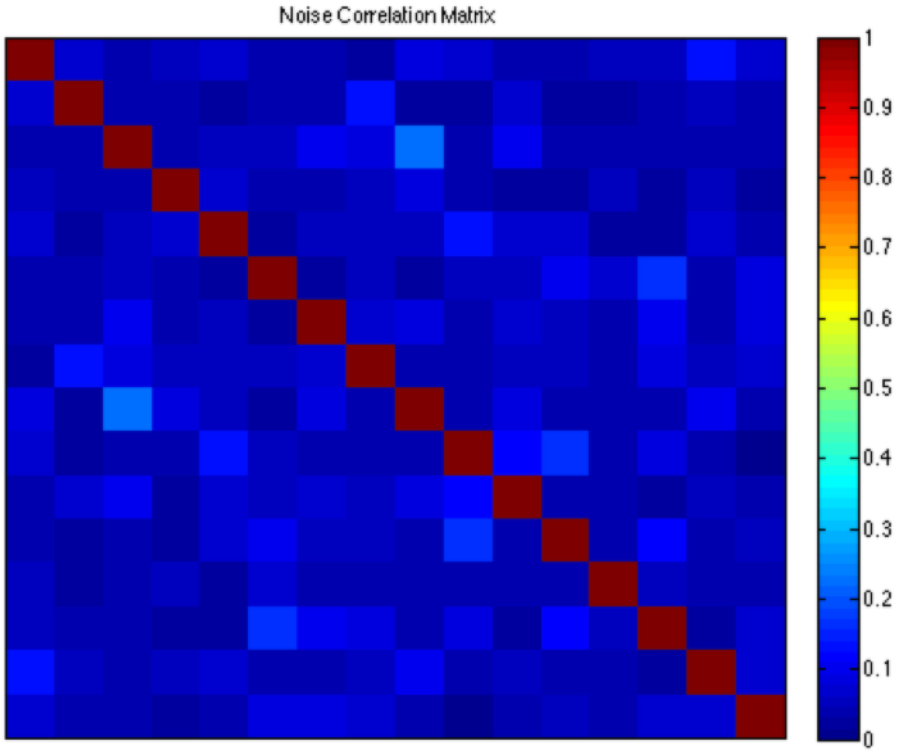

Figure 4.1: Noise correlation matrix. The noise correlation matrix demonstrates sufficient decoupling between elements (average: 5.7%, min: 1.36%, max: 22.61%).

Table 4.1: Reported Noise Correlation Matrices

	Mean	**Max**
Utrecht 7T unilateral 30 channel (20)	3.9% $\pm$ 2.9%	44%
Stanford 3T bilateral 16-channel (57)	12%	47%
3T 8-channel bilateral commercial coil (57)	34%	65%

IV.3 SNR

The noise-only scan also was used to calculate the SNR of the 16-channel receive array and the volume FCE coil. SNR is calculated as the ratio of the signal voltage to the noise voltage. The following theory is available in more detail in (77,78). For a single coil, the magnitude of the signal voltage can be defined as:

$$|V_{sig}| = \sqrt{2}\omega_0 \Delta V M_{xy} |B_t| \tag{4.1}$$

where ω is the Larmor frequency (rad/sec), ΔV is the volume of interest, M_{xy} is the transverse magnetization, and B_t is the RF flux density. The noise voltage, V_{noise}, is calculated as:

$$V_{noise} = \sqrt{4kT\Delta f R_{coil}} \tag{4.2}$$

where k is Boltzman's constant, T is the effective temperature, Δf is the bandwidth, R is the resistance of the coil. Using Eq. 4.1 and 4.2, the SNR can then be simplified to:

$$SNR = \frac{\sqrt{2}|B_t|}{\sqrt{R}} \tag{4.3}$$

For an array, the signal from each coil must be properly weighted to optimize SNR. With arrays, powers, rather than voltages, are considered since the weighting coefficients are optimized by the input power maximizing the effective flux density. The SNR of coil i of the array, including the weighting function, becomes:

$$SNR_i^2 = \frac{w_i^* w_i B_{ti}^* B_{ti}}{w_i^* w_i R_i} \tag{4.4}$$

where * denotes the complex conjugate (33). Weighting methods include sum of squares (27), B_1-weighted combining (27), or parallel imaging methods like SENSE (44).

For our measurements, SNR was calculated according to Kellman et al. in which the reconstructed images were scaled directly into SNR units (79). Data is acquired from a "dynamic scan" consisting of two scans with identical imaging parameters, but with the RF amplifiers turned on in one scan and off in the other to generate a noise-only scan (as described earlier). Using the image data from these two scans, an SNR map was generated and is shown in Fig. 4.2. A noise region of 30 mm x 30 mm coincident to the

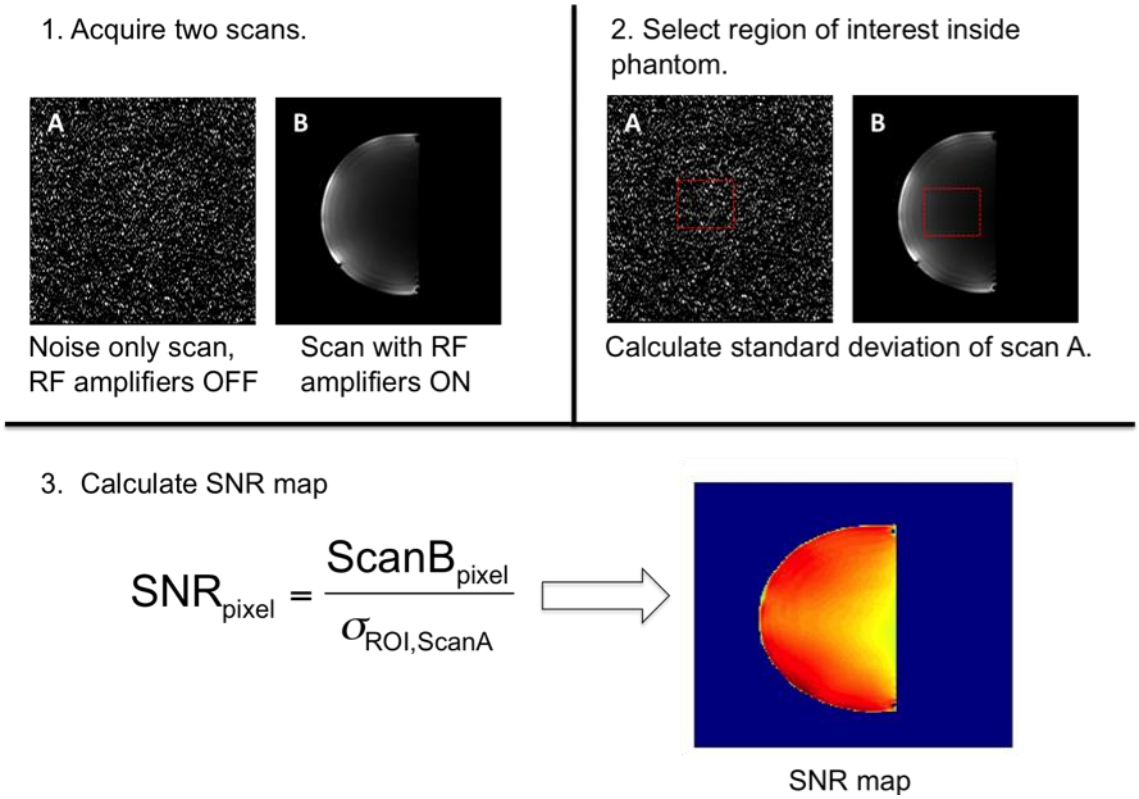

Figure 4.2: Step-by-step details for calculating SNR map**.** As proposed by Kellman et al., two scans are required: a noise-only scan with RF amplifiers off and an additional scan with RF amplifiers on. The spatial SNR map is the resultant of the second scan divided by the standard deviation of a region in the noise-only image.

phantom was chosen from the noise-only scan (20). Each pixel in the image was then calculated by taking the scan with the RF amplifiers on and dividing it with the standard deviation of the noise only region. The exact procedure with the same imaging parameters was repeated for the FCE volume coil in T-R mode for comparison.

Imaging was performed in the sagittal plane with the following scan parameters: TR = 6.0 ms, TE = 1.73 ms, flip angle = 8°, resolution of 1 x 1 x 2 mm^3 and bandwidth of 917.2 Hz. The SNR maps of a homogenous canola oil phantom are shown in Fig. 4.3, acquired both with the 16-channel receive array coil (right) and with the standalone volume coil with the array removed (left). The array provided an improved SNR throughout the entire phantom, achieving a mean SNR improvement of 6.5 times with up

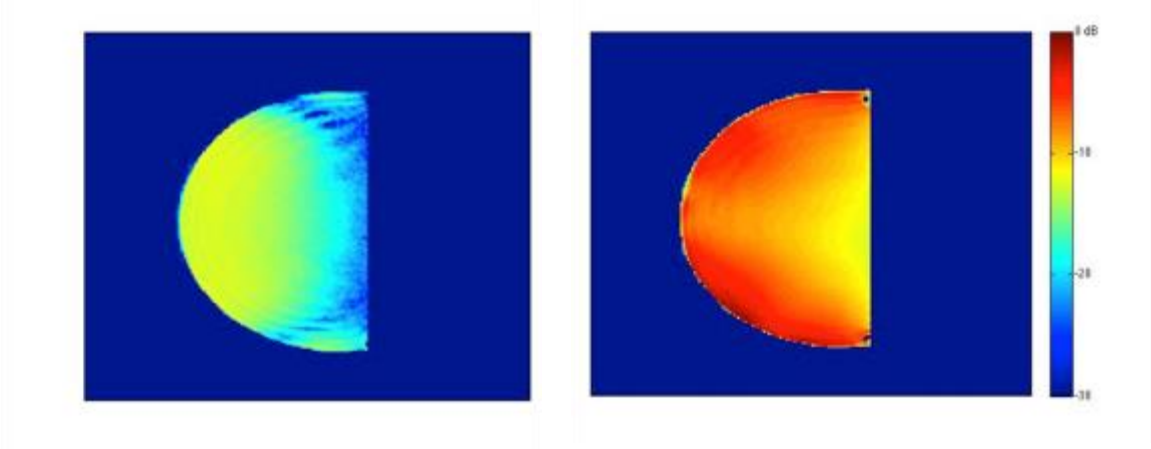

Figure 4.3: SNR maps of a homogenous canola oil phantom acquired with the volume coil (left) and the 16-channel receive array (right). Sagittal view is shown. Both maps were normalized to the maximum SNR from the 16-channel receive array (0 dB=1583 a.u. SNR). The 16-channel receive array demonstrates a mean SNR improvement of 6.5.

to a 12.8 times increase at the edges. As expected, the array sensitivity steadily decreased with distance into the phantom (77), yet a 2.5-fold increase in SNR was achieved at the center. The slight inhomogeneity evident along the edges could be due, in part, to the standard constructive and destructive interference patterns seen at 7T (80). The maps were normalized to the maximum SNR from the 16-channel receive array (0 dB=1583 a.u. SNR) and clearly demonstrate the dramatic increase in SNR provided by the array. SNR profiles of both coils are displayed in Fig. 4.4 to better quantify the SNR through the phantom.

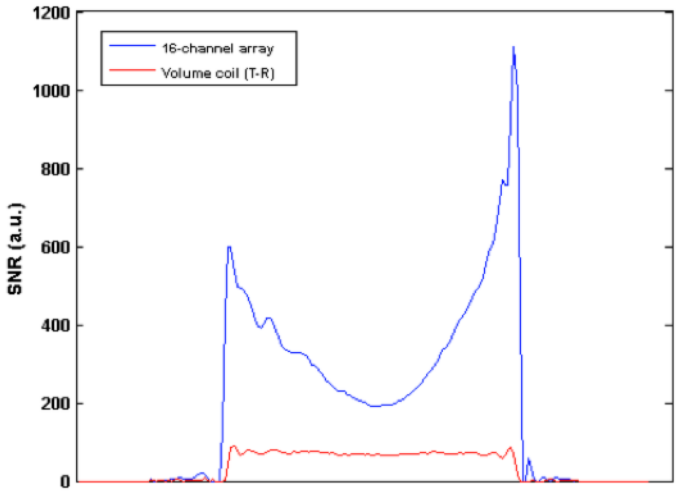

Figure 4.4: SNR profiles from the 16-channel receive array (blue) and the volume coil in T-R mode (red). The same column was extracted from each image for the comparison.

IV.4 *g*-factor Evaluation

In SENSE imaging (described in Ch. II), as with all parallel imaging techniques, acceleration of scan time is achieved by eliminating the acquisition of a portion of the raw MRI data (k-space lines). The resulting aliased image is then "unfolded" using the known coil sensitivity maps to yield a full FOV reconstructed image. Since the individual coils are positioned differently across the FOV, the coil sensitivities, and effectively the *g*-factor, vary pixel-by-pixel and are presented in the form of a *g*-factor map. *g*-factor maps are a measure of the ability of the array coil to accelerate with respect to the expense to SNR. The ideal *g*-factor is 1, with high *g*-factors corresponding to dramatic losses in SNR and reduced parallel imaging performance.

The *g*-factor maps for the 16-channel array are shown in Fig. 4.5, obtained using SENSE reduction factors up to nine-fold in two directions. To generate the *g*-factor maps, a full dataset with no acceleration, an accelerated dataset, and necessary noise measurements for calculating SNR were required. We acquired a series of accelerated datasets with acceleration factors of 1x, 2x or 3x in the foot-to-head (F/H) direction along with 1x, 2x or 3x acceleration in the left-to-right (L/R) direction. The *g*-factor map can then be generated with the SNR of the reduced image SNR_{red}, the unaccelerated SNR image SNR_{full} and the reduction factor *R*, as shown previously in Eq. 2.6 and repeated here for convenience:

$$g = \frac{SNR_{full}}{SNR_{red} * \sqrt{R}} \tag{4.5}$$

Table 4.2 lists the mean and maximum *g*-factors and the scan time for each accelerated image, with a mean g-factor of 1.31 for the maximum acceleration of 3x3. There is some discrepancy in literature as to the maximum tolerable/useful *g*-factor value. Larkman has stated it is generally accepted that an SNR loss of up to 20% (*g*-factor 1.2) is considered acceptable (80,81). This condition was maintained for total accelerations through six, corresponding to a reduction in imaging time from 49.7 sec to 10.5 sec. This limit is somewhat arbitrary, however, and higher tolerances have been applied (82,83). For breast imaging specifically, Nnewihe et al. considers low mean *g*-factors to go up to 1.5 (57); Marshall et al. reported up to a bidirectional acceleration of R=4 with a 16-channel bilateral breast array at 1.5T, with a mean *g*-factor of 1.01 (58); van de Bank et al. reported a maximum mean *g*-factor of 1.46 for their 7T 30-channel array (20).

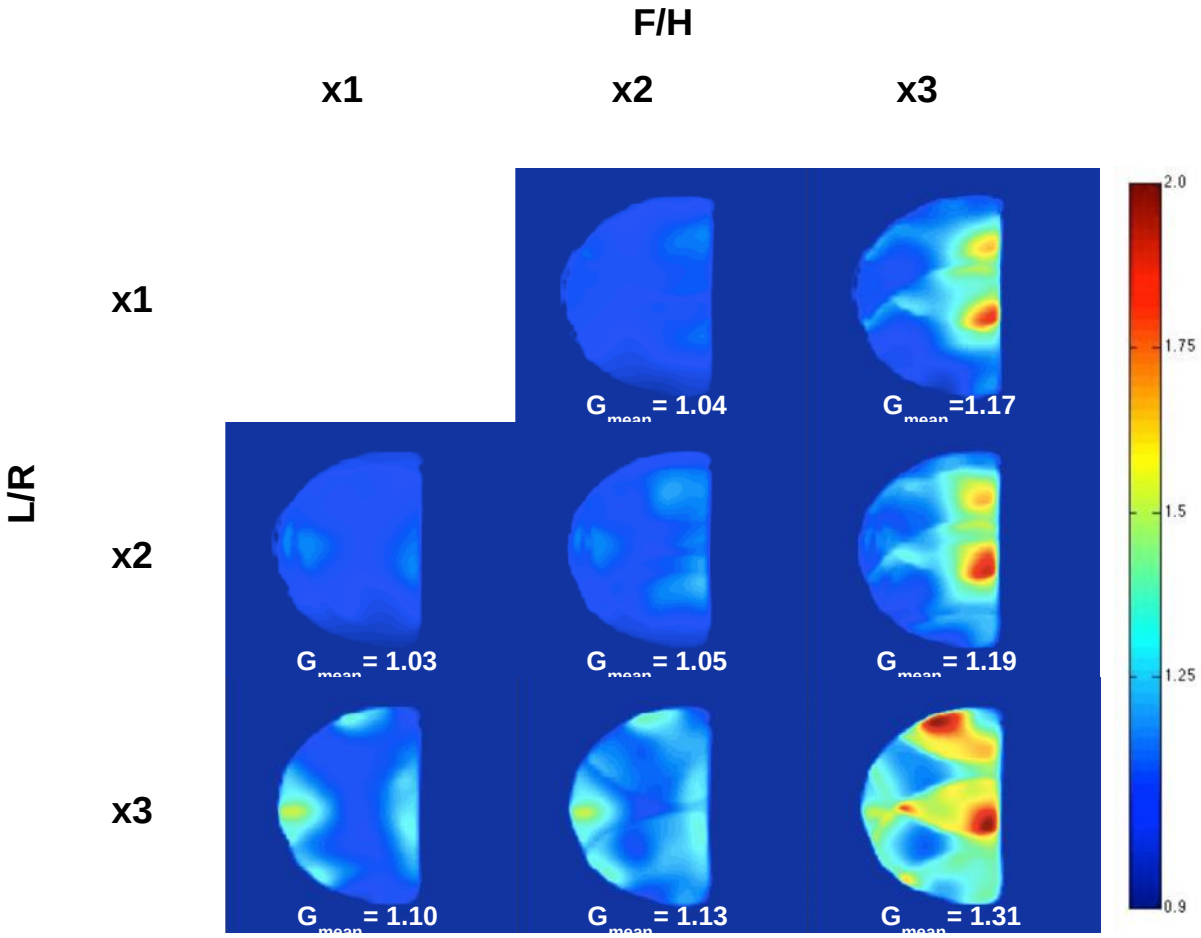

Figure 4.5: *g*-factor maps of a sagittal slice up to a nine-fold (F/H x L/R = 3 x 3) reduction factor. SENSE acceleration was applied in the left to right (L/R) and foot to head (F/H) directions using reduction factors of 1x, 2x, or 3x in each direction. With R = 9, the mean *g*-factor was 1.31 and the maximum *g*-factor was 2.

Table 4.2: *g*-factors and Scan Times

F/H **L/R**	**1**	**2**	**3**
1	Ref scan Scan Time: 49.7 sec	G_{mean}=1.04 G_{max}=1.14 Scan Time: 26.9 sec	G_{mean}=1.17 G_{max}=1.81 Scan Time: 19.2 sec
2	G_{mean}=1.03 G_{max}=1.15 Scan Time: 27.4 sec	G_{mean}=1.05 G_{max}=1.21 Scan Time: 15.5 sec	G_{mean}=1.19 G_{max}=1.91 Scan Time: 11.4 sec
3	G_{mean}=1.10 G_{max}=1.52 Scan Time: 17.3 sec	G_{mean}=1.13 G_{max}=1.50 Scan Time: 10.5 sec	G_{mean}=1.31 G_{max}=2 Scan Time: 7.8 sec

IV.5 Individual Field Patterns

From the same SNR scans as described earlier in IV.3, we generated individual field patterns for each element of the array. These field patterns served as another measure of isolation between elements, albeit a qualitative one. The individual field patterns for each receive element were generated using OsiriX, an open-source PACS

Workstation DICOM viewer. The final results for the individual field patterns are shown in Fig. 4.6.

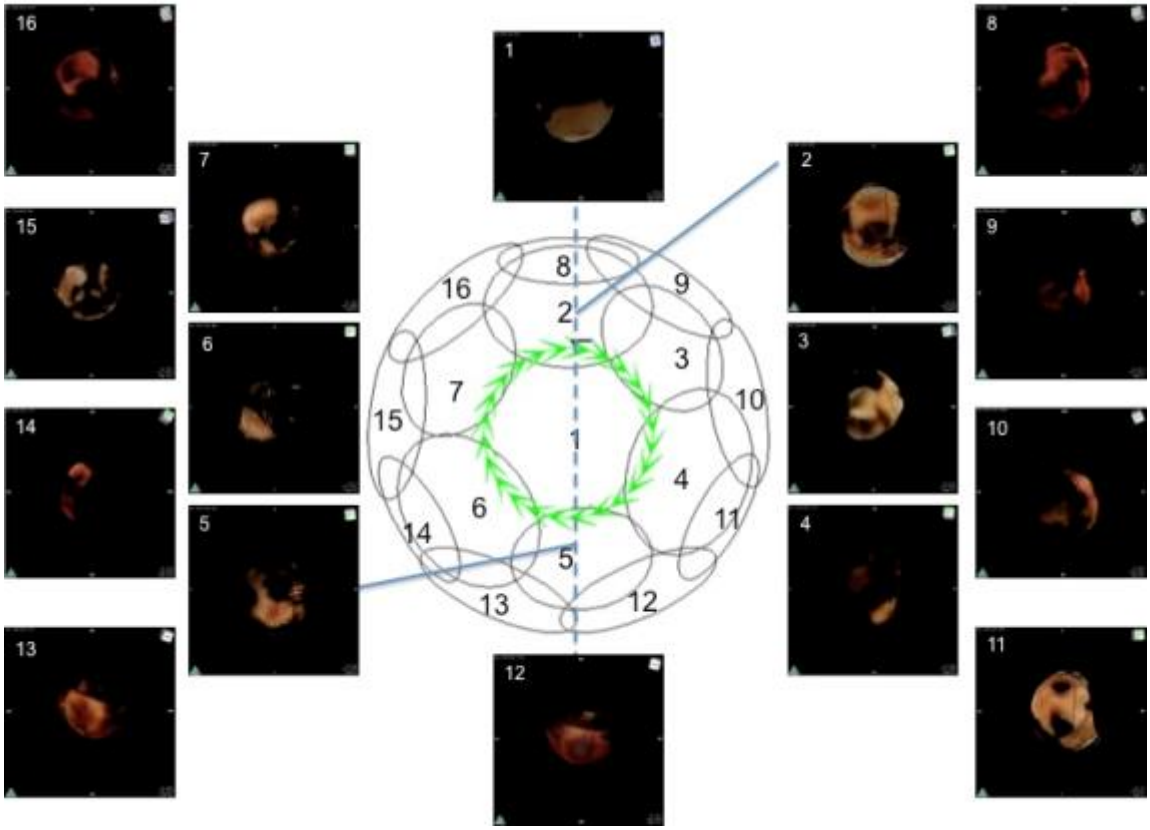

Figure 4.6: 3D volume renderings for individual elements in the array.

It is clear that there is still some residual coupling in some channel. To assess the source of potential coupling, we tested three primary concerns: insufficient receive array decoupling, incorrect receive array cable lengths, and insufficient transmit decoupling.

IV.5.1 Testing of Receive Array Decoupling

Failure of traps under power would result in insufficient decoupling of the receive coils during transmit. A gradient echo sequence, which decreases power by 6 dB in comparison to a spin echo sequence, with a very low tip angle was used to help assess array patterns without worrying if the traps were being damaged or being switched on with applied RF. If this were the source of the problem, we would expect to see localized patterns in the low power scan (i.e. one bright spot for each channel indicating the location of the coil). For the purposes of demonstration, sagittal slices of only channels 2 and 8 are shown in Fig. 4.7. Though the reconstructed image did not raise any concerns, the individual channel images still indicated problems. The additional bright spots from several other areas in both reconstructed channels indicated that coupling was still present when the power was reduced.

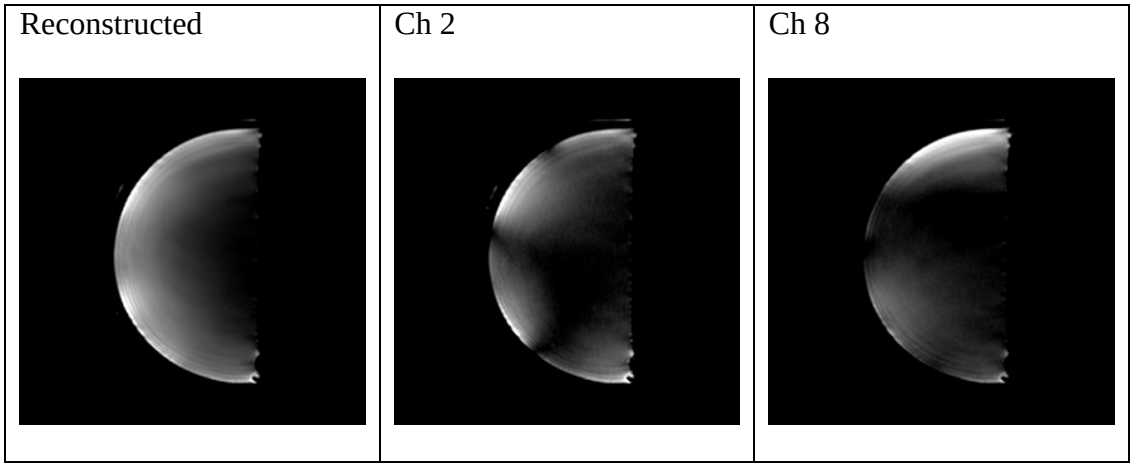

Figure 4.7: Results from low power scan. A gradient echo was used to assess whether traps were failing under power. Reconstruction of individual channels indicated that coupling was still present when the power was reduced.

As an additional test, to ensure a uniform field was being transmitted with the array insert in place, a field map of a homogenous canola oil phantom was acquired. The default state of the Philips receiver box is -5V, ensuring that all of the receive array elements are detuned during this scan. The map was acquired in the sagittal plane with the FCE volume coil driven in quadrature mode using a 50° flip angle, TE of 3 ms and TR of 35 ms. Despite the additional copper loading from the array, the transmit coil was still highly homogenous throughout the entire phantom, indicating that the traps on the receive elements were successfully decoupling the element during receive. The B_1^+ field map and profiles from the FCE breast coil are shown in Fig. 4.8 below. $B_1^+$is shown as a percentage of the nominal tip angle of 50°. The plots indicate that inside the phantom the B_1^+ field at most varies only by 3.3% and 3.2% on the vertical (S-I) and horizontal (A-P) axis respectively.

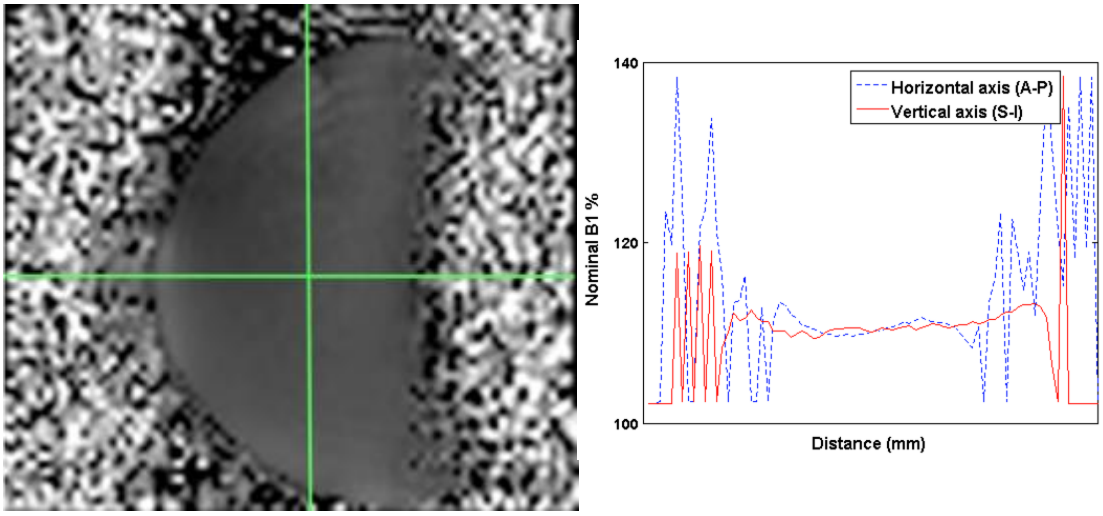

Figure 4.8: $\boldsymbol{B_1^+}$field map (left) with relative line plots (right). The presence of the array did not deteriorate the homogeneity of the transmit field.

IV.5.2 Testing for Incorrect Receive Array Cable Lengths

As described in Chapter III, the preamplifiers serve as the main source of element-to-element decoupling for non-nearest neighbors and as a source of increased decoupling in addition to geometric overlap for nearest neighbors. The cable length between the coil and the preamplifier is crucial, as incorrect lengths would no longer present a low impedance to the trap at the coil. To test this concern, 15 receive coils were physically shorted by soldering a wire at the end of the transmission line on the trap board. One receive element (coil 2, chosen at random) was not shorted in order to be used to receive. This coil was the only coil plugged into the Philips receiver box, and all the other ports on the receiver box were terminated with a 50 Ω load. This ensured a scan receiving with only one element with all other elements "ideally" decoupled, removing any potential effect of an incorrect cable length connecting to the preamplifier. Figure 4.9 includes the reconstructed full and channel 2 image results from this scan.

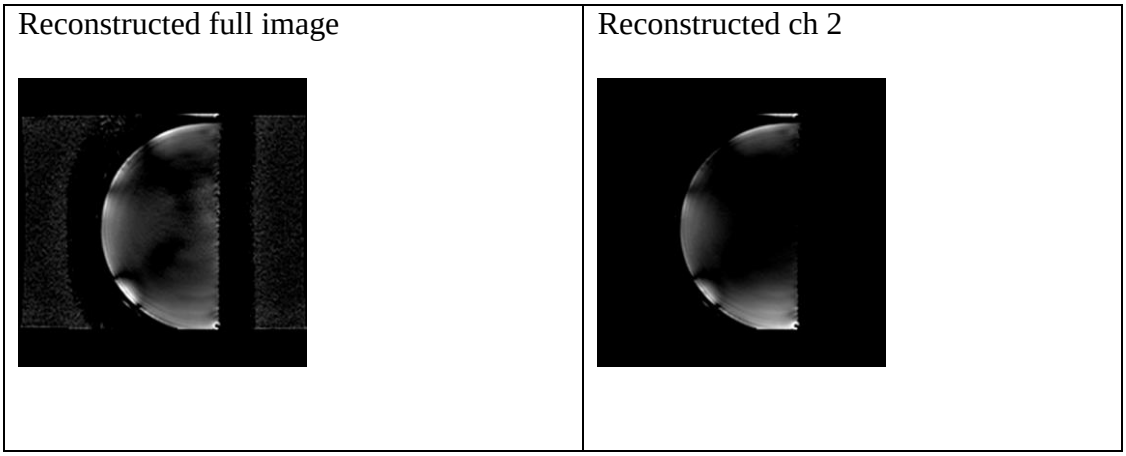

Figure 4.9: Results when receiving with only channel and other channels shorted. The results indicate that the receive array cable lengths do not seem to be the source of coupling.

Even with the other channels disconnected from the receiver but physically shorted, the reconstructed channel 2 resembled the reconstruction in the previous experiment (Fig. 4.7) and demonstrated that element-to-element coupling was still significant and not an effect of traps failing under power or of incorrect cable lengths connecting to the preamplifiers.

During this test, one potential source of coupling, albeit small, was observed in the Philips receiver box itself. Though there should have been only noise on all channels other than channel 2 (because they were terminated with a 50 Ω load), we reconstructed the neighboring channels 1 and 3 and the results are shown in Fig. 4.10.

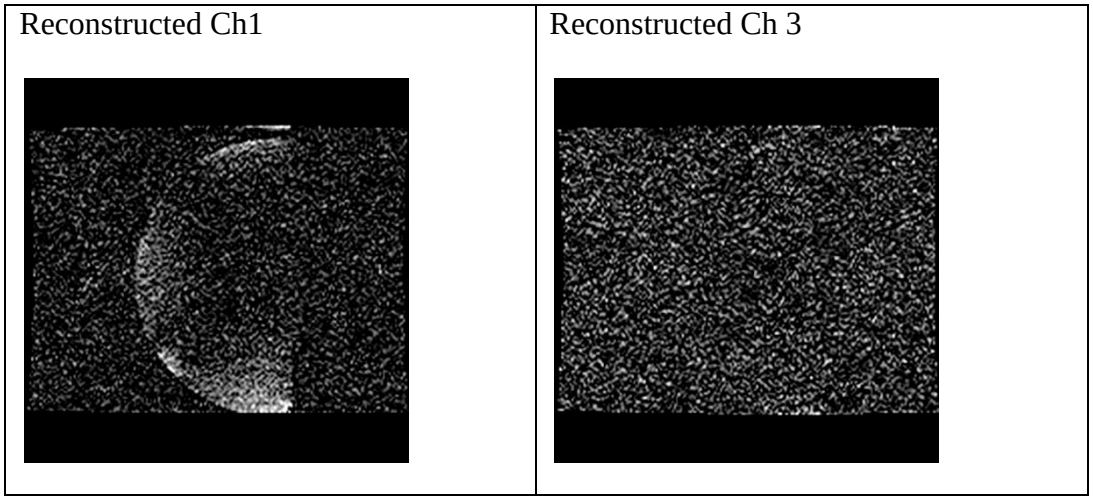

Figure 4.10: Reconstruction of neighboring channels. With only channel 2 receiving, all other channels of the receiver box were terminated with a 50 Ω load. We expect to see noise in all other reconstructed channel images, but the outline of the phantom is visible.

The phantom was evident in the channel 1 reconstruction and the outline of the phantom was slightly visible in the channel 3 reconstruction. The individual image for channel 7 (a non neighboring element to channel 2) was also reconstructed and included only noise, as expected. This data revealed some coupling within neighboring elements inside the Philips preamplifier box. The box is arranged in two rows of eight channels and Stacked channels were not affected (i.e. channels 1 and 9, channels 2 and 10, etc.) in the same manner as adjacent channels. While the amount of coupling observed in the receiver box was not enough to explain the significantly coupled single channel images, it was unexpected and worth noting.

IV.5.3 Testing for Insufficient Transmit Coil Decoupling

With no clear indication that element-to-element coupling was occurring on the "receive side", we investigated the transmit coil. While transmit decoupling appeared to be sufficient on the bench through field measurements, verification of its feasibility under power was needed. To simplify the testing, only element 14 was used to receive. All other elements were open-circuited by removing the trap boards from their corresponding elements, which effectively removed the match capacitor from each receive coil. Receive coil 14 was connected to the receiver box, and all other ports were terminated with a 50 Ω load. A vial of canola oil was placed at the center apex of the array shell (which corresponds to the center of receive coil 1) in order to have a quantitative measure based on the SNR of the vial. Since the vial is located far away from receive coil 14, we did not expect any signal in the vial unless it was coupling through the transmit coil.

Two images were acquired: an image with the transmit detuning active and another with the PIN diodes removed from the common voltage point (CVP) of both transmit elements to disable transmit detuning. We expected to see a significant difference in these two images, because without the transmit detuning, the transmit coil would couple with receive element 14. These results are shown in Fig. 4.11 below.

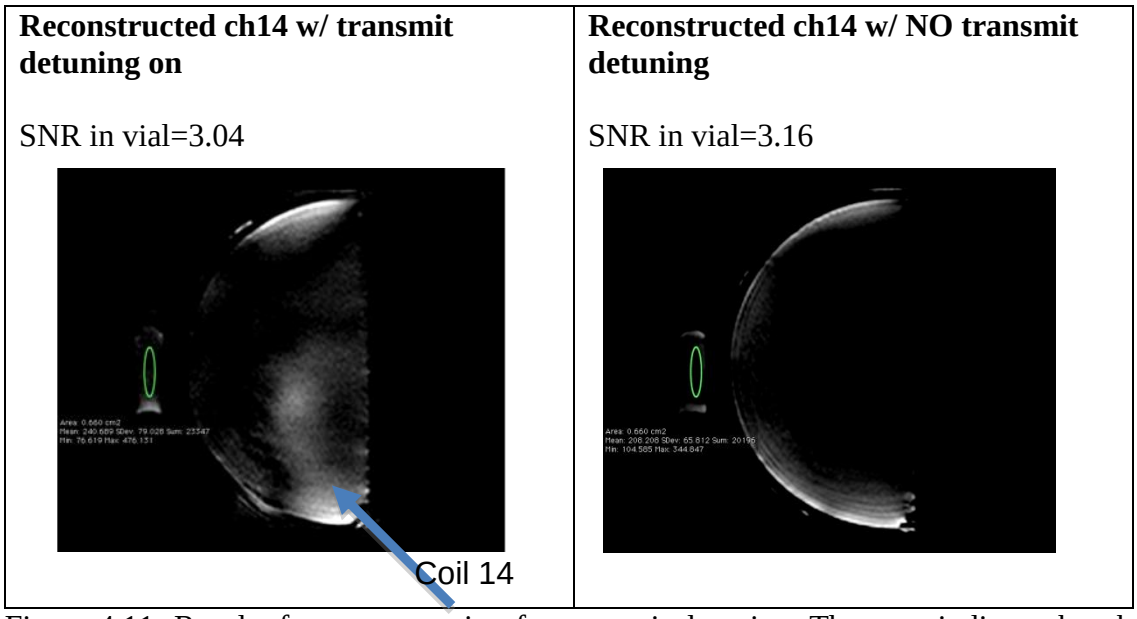

Figure 4.11: Results from scan testing for transmit detuning. The tests indicate that the transmit coil is at least partially detuning, but is likely the problem for the coupling patterns evident in the individual receive element field patterns.

It is clear that the patterns are different with and without the transmit detuning, as expected. However, the most significant point to note was that the vial located a distance away from the receive coil 14 generated nearly equal signal in both images, indicating that the transmit coil was at least partially "receiving" via coupling in both cases,

including when it was “detuned”. As an additional indicator, there were bright spots throughout the phantom even though all the trap boards were removed.

These tests indicate that the transmit coil is most likely the problem for the coupling patterns in the individual receive element field patterns. Changing anything extensive on the transmit side was outside the scheme of this work, especially because of the strong performance of the receive array in terms of noise correlation, SNR and g-factor. This, however, represents an immediate area of improvement for future work.

IV.6 Conclusion

In conclusion, we have demonstrated the benefits of the 16-channel receive array insert over the volume coil in terms of SNR and have shown its ability to accelerate imaging via noise correlation matrices and g-factor performance. In a phantom, the array provided a 6.5 time improvement in mean SNR over the volume coil, providing the ability to increase resolution or decrease scan time depending on the application at hand.

CHAPTER V

IN VIVO IMAGING

This chapter presents the initial in vivo images acquired with the 16-channel receive array insert. First, the methods for temperature mapping are detailed. The chapter progresses by presenting both unaccelerated and accelerated in vivo images acquired with the 16-channel receive array insert to demonstrate the utility of the array in a clinical environment.

V.1 Temperature Mapping for the 16-Channel Receive Array

Two temperature mapping experiments were conducted to observe coil heating and are described below.

V.1.1 IR Imaging

A thermal test system was constructed to simulate a clinical setting for exciting the coil. The test system consisted of a 300 MHz source (a network analyzer), a 300 watt amplifier and a circulator to protect the amplifier. The coil under test was excited in the test chamber (RF shielded) for 30 minutes and heating was measured before and after excitation through infared (IR) imaging with a FLIR Systems FLIR-17 thermal camera. The IR camera, however, is extremely sensitive to reflectance, and consequently, calibration. Therefore, it is not intended as a quantitative indicator of operation within FDA approved guidelines. Instead, it is a relative indicator of heating used to track down hot spots (i.e. failed coils, baluns, highly coupled areas).

The quadrature FCE transmit coil was excited with the receive array detuned using the 16-channel "fan-out" board to send -5V from a power supply to each of the channels. All of the passive traps on the receive array were physically shorted. These thermal tests used a saline phantom to mimic the chest wall and a canola oil phantom to fill the shell. The transmit coil was subjected to 30 minutes of 300 W rectangular pulses, 25 msec repetition rate and 3 msec pulse duration. This corresponds to a 12% duty cycle and an average power of 36 W, which is greater than would be expected clinically. The results of the thermal testing are shown in Fig. 5.1 below. The top row includes a picture of the phantom in visible light. The before and after images demonstrate no significant heating; the "hot" areas on the sides of the shell were verified to be misconstrued as a result of reflectance by observing the "hot" areas at different angles with the FLIR camera.

V.1.2 Calorimetry Readings

Fiber optic probe based measurements of phantom heating was done at University of Texas Southwestern Medical Center (UTSW). Calorimetry readings with temperature sensors in various locations throughout the phantom were recorded. The same 3D THRIVE pulse sequence intended for use during the human scans was run for 10 minutes. For the trunk specifically, the FDA specifies that localized heating cannot exceed 2°C over any period of 5 minutes (84)**.** Table 5.1 lists the calorimetry readings for various positions in the array, indicating that no significant heating is expected.

Visible Light	
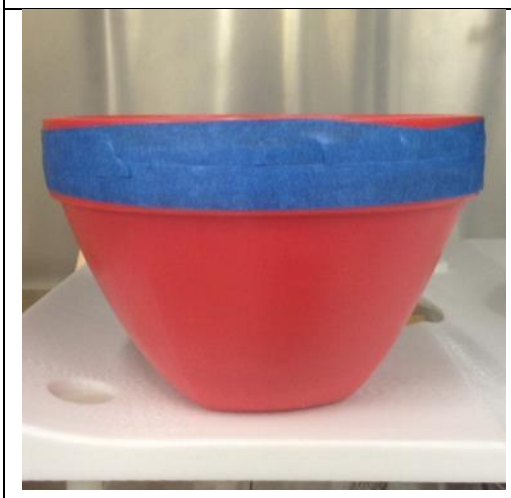	
Before Heating	**After 30 Minutes of Heating**
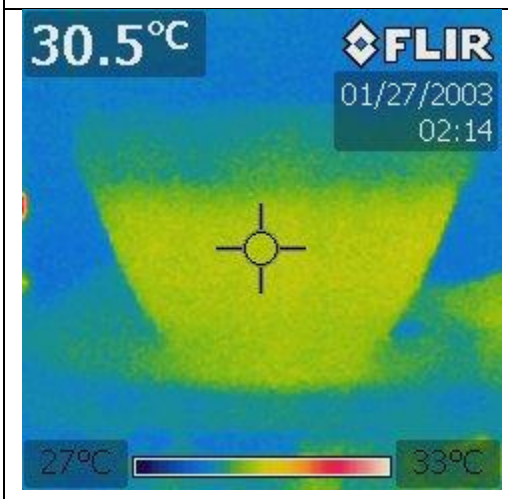	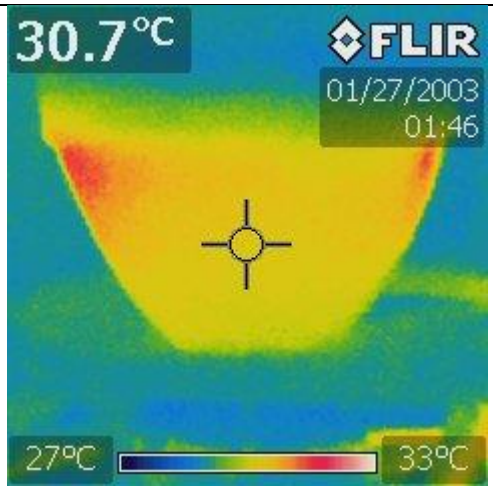

Figure 5.1: Visible and thermal images of a breast canola oil phantom. Thermal images were obtained with a FLIR-17 camera before and after 30 minutes of heating.

Table 5.1: Calorimetry Readings for Temperature Mapping

Position on Array	**Temperature Increase**
Inside shell, on side of saddle feed area	0.4° C
Inside shell, near feed point of HH/passive traps	0.2° C
Inside shell at apex, center of coil 1	No Increase

V.2 Imaging

Imaging was performed under a protocol approved by the local IRB and after obtaining written informed consent. The subjects were in prone position with the head resting on pillows and with arms either to the side or above the head. In vivo images were obtained with and without acceleration with the 16-channel receive array insert using a 3D THRIVE sequence with fat suppression. Fat suppression was acquired using SPectral Attenuated Inversion Recovery (SPAIR).

V.2.1 Unaccelerated

An image with 1 mm isotropic spatial resolution is presented in all three planes in Fig. 5.2, demonstrating excellent fat suppression and the high level of available detail. The axial view shows the achievable penetration into the chest wall with the receive array. Total scan time was 2:01 minutes, but this also included the dynamic noise scan, which would not be performed in a clinical situation.

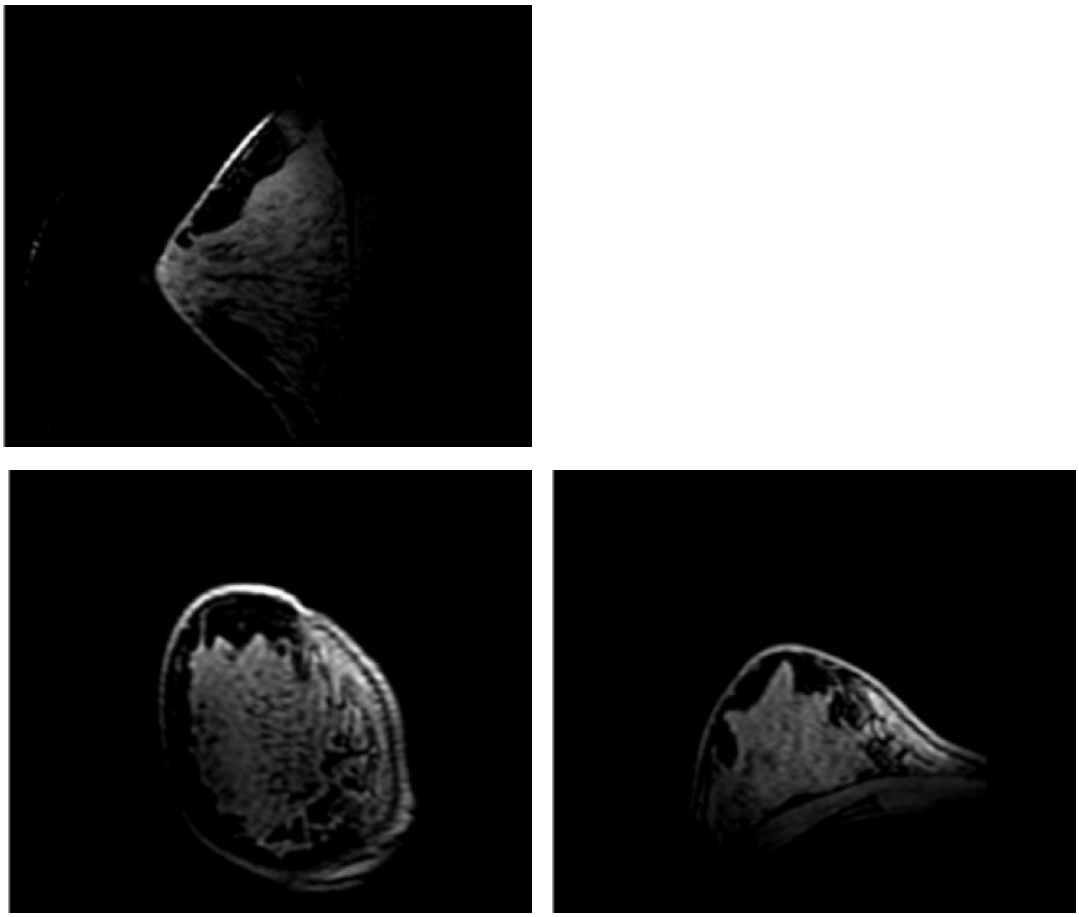

Figure 5.2: 1x1x1 mm^3 image of a volunteer in all three planes (top left: sagittal, bottom left: coronal, bottom right: axial).

V.2.2 Accelerated

Figure 5.3 shows a sagittal slice of the breast, with increasing SENSE acceleration from R=2 to R=4. For R=2 and R=3, SENSE was only applied in the F/H direction. In the bottom image, which was acquired with a SENSE acceleration factor of

R=4, bidirectional acceleration was applied in both the L/R and F/H (x2 in each direction). Each image had a voxel size of 1 mm^3 and the respective times for these scans are listed in the image. As the acceleration factor increases, there is a decrease in acquisition time, but a degradation in resolution is seen. There is a 25% degradation in SNR when increasing the reduction factor from R=2 to R=3. The SNR for R=4 was not calculated, because a noise-only scan was not acquired for this image.

Figure 5.4 shows a high resolution accelerated image (.5 mm^3) of SENSE of 3 applied in the F/H direction. Using the benefit of the SNR achievable with the array, very high resolution in vivo imaging was performed. Standard clinical resolutions have an in-plane resolution of 1 mm and standard scan times are generally under 3 minutes (12). An example image is shown in Figure 5.4. In this case, .5 mm isotropic resolution was achieved in 1:28 minutes using a SENSE of 3 in the F/H direction.

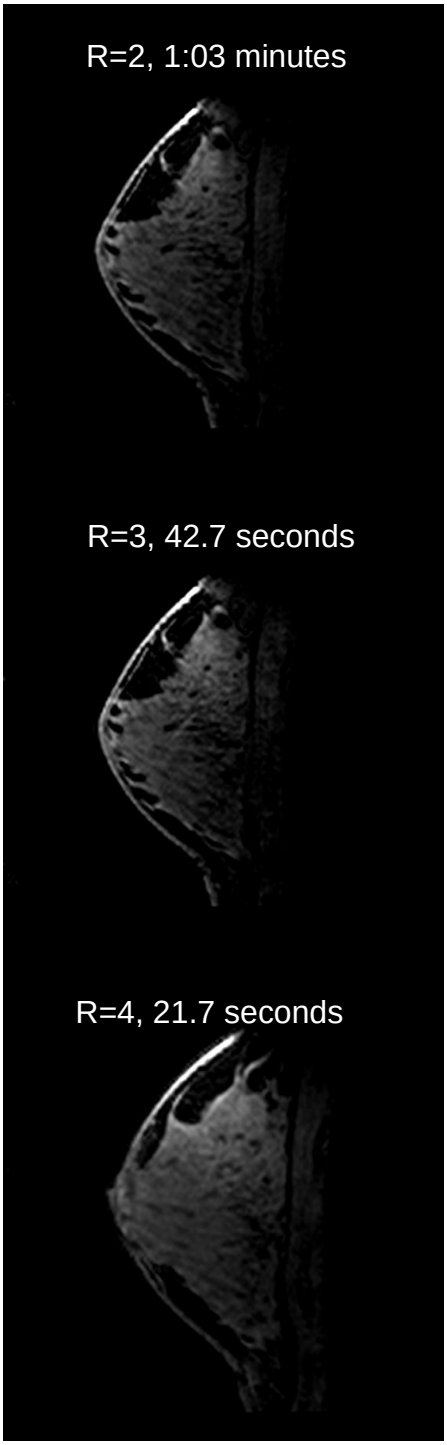

Figure 5.3: Breast images with increasing acceleration factors. SENSE was applied in the F/H direction for R=2 and R=3. For R=4, SENSE of 2 was applied in both L/R and F/H directions. A spatial resolution of 1 mm isotropic was achieved.

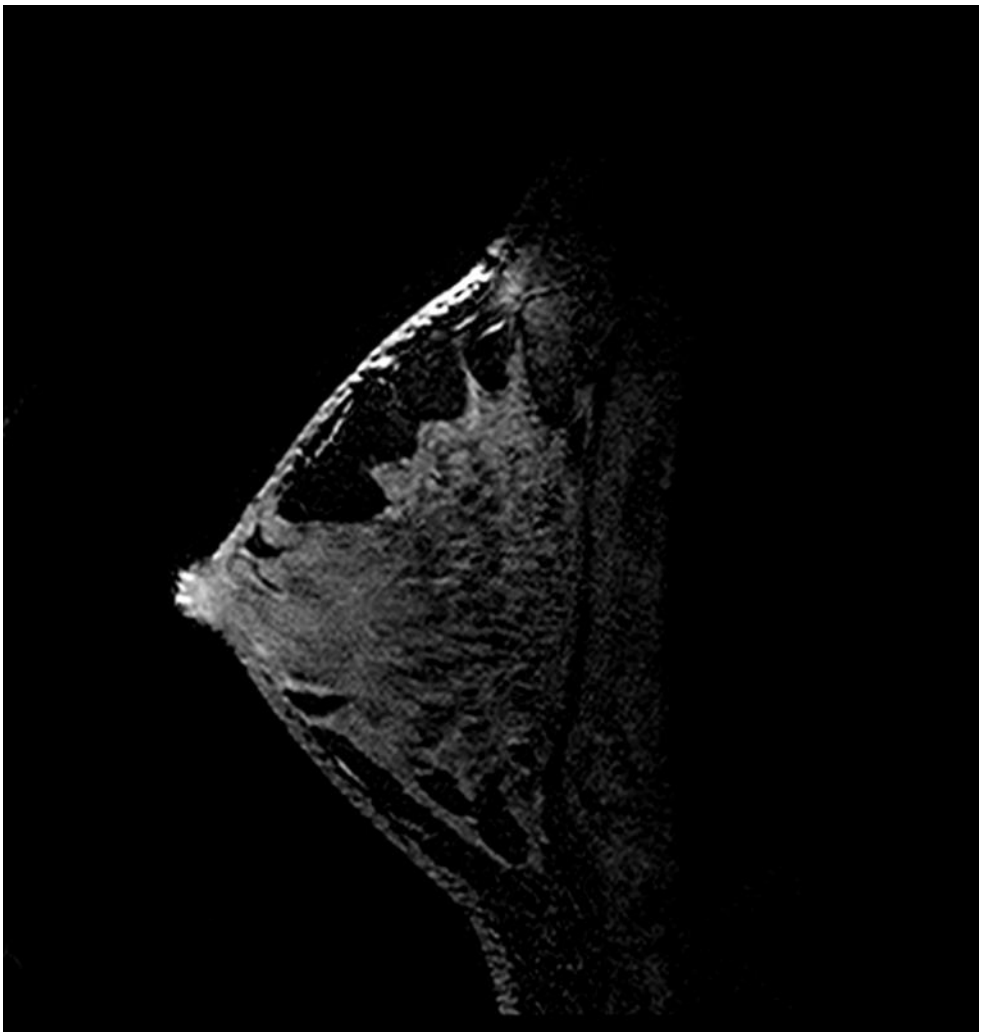

Figure 5.4: Ultra high resolution breast image with a SENSE of 3. Image acquired with a resolution of .5x.5x.5mm^3

CHAPTER VI

CONCLUSIONS AND FUTURE WORK

The objective of this work was to enable high resolution breast images at 7T with the potential to perform acceleration. To do so, we designed, constructed and evaluated a dedicated 16-channel receive array for use inside a quadrature FCE volume coil. In comparison to the quadrature FCE volume coil in T-R mode, the 16-channel receive array insert achieved an increase in mean SNR of 6.5x and the ability to accelerate in two directions. In addition to phantom imaging, the array was tested in vivo. Initial imaging demonstrated excellent delineation of the breast with very high resolutions of .5 mm isotropic.

Further improvements on the array design could improve overall performance in future versions. Constructing the coils out of wire rather than etching them on PCB has been shown to be "optimal" (69). Another potential improvement includes implementing co-planar shields on each element (85-87). We have done preliminary testing on the effects of element shielding on receive-only arrays at 7T and the results indicated advantages in terms of SNR, *g*-factor, and transmit power efficiency (88). Since the focus of the current work is on the understanding of the disease, seeing into the chest wall wasn't emphasized or considered a priority. However, it is worth nothing that penetration into the chest wall and axilla are important for breast imaging and will be needed for clinical translation. Finally, the most obvious improvement would be to modify the receive array for bilateral use. During the course of this project, the receiver

system at UTSW was upgraded to a 32-channel system, enabling the option to add another 16 channels in a bilateral configuration.

The developed hardware was built with the number of scientific opportunities it could enable in mind. One application is improving the diagnosis of breast cancer. For example, the presence of microcalcifications is strongly associated with ductal carcinoma in situ (DCIS). Often, this pre-invasive cancer goes undetected when using standard dynamic contrast enhanced MRI protocols. Susceptibility weighted imaging (SWI) has been proposed as a method to detect breast microcalcifications, but currently, SWI is not possible on clinical scanners due to the long acquisition times required to obtain ultra high resolutions. The increased SNR provided by the array in addition to the inherent SNR increase at 7T, however, makes SWI more feasible (89).

Spectroscopy performance can also take advantage of the benefits provided by the 16-channel receive array. With the increased resolution, we can study the role of different metabolites in breast cancer. Choline is a metabolite of interest, as it may indicate the malignancy of a breast tumor. With the enhanced sensitivity of the 16-channel array, choline detection via ^{1}H spectroscopy can be improved.

Overall, the major contributions of this work were, and will continue to be, in concert with the efforts to better understand, prevent and treat breast cancer.

REFERENCES

1. American Cancer Society, Inc. Cancer facts & figures 2013; 2013.

2. Siegel R, Naishadham D, Jemal A. Cancer statistics, 2013. CA: A Cancer Journal for Clinicians 2013;63(1):11-30.

3. Saslow D, Boetes C, Burke W, Harms S, Leach M, Lehman C, Morris E, Pisano E, Schnall M, Sener S, Smith RA, Warner E, Yaffe M, Andrews KS, Russell C. American Cancer Society guidelines for breast screening with MRI as an adjunct to mammography. CA: A Cancer Journal for Clinicians 2007;57(2):75-89.

4. Bluemke DA, Gatsonis CA, Chen MH, DeAngelis GA, DeBruhl N, Harms S, Heywang-Köbrunner SH, Hylton N, Kuhl CK, Lehman C, Pisano ED, Causer P, Schnitt SJ, Smazal SF, Stelling CB, Weatherall PT, Schnall MD. Magnetic resonance imaging of the breast prior to biopsy. Journal of the American Medical Association 2004;292(22):2735-2742.

5. Drew PJ, Turnbull LW, Chatterjee S, Read J, Carleton PJ, Fox JN, Monson J, Kerin MJ. Prospective comparison of standard triple assessment and dynamic magnetic resonance imaging of the breast for the evaluation of symptomatic breast lesions. Annals of Surgery 1999;230(5):680-685.

6. Fischer U, Kopka L, Grabbe E. Breast Carcinoma: Effect of Preoperative Contrast-enhanced MR imaging on the therapeutic approach. Radiology 1999;213(3):881-888.

7. Teifke A, Hlawatsch A, Beier T, Vomweg TW, Schadmand S, Schmidt M, Lehr H-A, Thelen M. Undetected malignancies of the breast: Dynamic contrast-enhanced MR imaging at 1.0T. Radiology 2002;224:881-888.

8. Kuhl CK, Schild HH. Dynamic image interpretation of MRI of the breast. Journal of Magnetic Resonance Imaging 2000;12(6):965-974.

9. Kriege M, Brekelmans CTM, Boetes C, Besnard PE, Zonderland HM, Obdeijn IM, Manoliu RA, Kok T, Peterse H, Tilanus-Linthorst MMA, Muller SH, Meijer S, Oosterwijk JC, Beex LVAM, Tollenaar RAEM, de Koning HJ, Rutgers EJT, Klijn JGM. Efficacy of MRI and mammography for breast-cancer screening in women with a familial or genetic predisposition. New England Journal of Medicine 2004;351(5):427-437.

10. Lehman CD, Gatsonis C, Kuhl CK, Hendrick RE, Pisano ED, Hanna L, Peacock S, Smazal SF, Maki DD, Julian TB, DePeri ER, Bluemke DA, Schnall MD. MRI

evaluation of the contralateral breast in women with recently diagnosed breast cancer. The New England Journal of Medicine 2007;356(13):1295-1303.

11. Berg WA, Gutierrez L, NessAiver MS, Carter WB, Bhargavan M, Lewis RS, Ioffe OB. Diagnostic accuracy of mammography, clinical examination, US, and MR imaging in preoperative assessment of breast cancer. Radiology 2004;233(3):830-849.

12. American College of Radiology. ACR practice guideline for the performance of contrast-enhanced magnetic resonance imaging (MRI) of the breast. http://www.acr.org; 2013.

13. Korteweg MA, Veldhuis WB, Visser F, Luijten PR, Mali WPTM, van Diest PJ, van den Bosch MAAJ, Klomp DJ. Feasibility of 7 tesla breast magnetic resonance imaging determination of intrinsic sensitivity and high-resolution magnetic resonance imaging, diffusion-weighted imaging, and 1H-magnetic resonance spectroscopy of breast cancer patients receiving neoadjuvant therapy. Investigative Radiology 2011;46(6):370.

14. Theysohn JM, Maderwald S, Kraff O, Moenninghoff C, Ladd ME, Ladd SC. Subjective acceptance of 7 tesla MRI for human imaging. Magnetic Resonance Materials in Physics 2008;21:63-72.

15. Vaughan JT, Snyder CJ, DelaBarre LJ, Bolan PJ, Tian J, Bolinger L, Adriany G, Andersen P, Strupp J, Ugurbil K. 7 T Whole-body imaging: Preliminary results. Magnetic Resonance in Medicine 2008;61(1):244-248.

16. Brown R, Megorty K, Moy L, DeGregorio S, Sodickson D, Wiggins GC. Sub-millimeter breast imaging and relaxivity characterization at 7T. In: Proceedings of the 19th Annual Meeting of ISMRM. Montréal, Canada, 2011. p 3092.

17. Cheshkov S, Dimitrov I, Rispoli JV, Gonzales E, Malloy C, McDougall MP, Wright SM. Proton decoupled 13C MRS of the breast at 7T. In: Proceedings of the 20th Annual Meeting of ISMRM. Melbourne, Australia, 2012. p 1783.

18. Dimitrov I, Madhuranthakam A, Cheshkov S, Seiler S, Goudreau S, Rispoli JV, McDougall MP, Wright SM, Malloy C. BreastView: Isotropic 3D high resolution T2-weighted breast imaging at 7T. In: Proceedings of the 21st Annual Meeting of ISMRM. Salt Lake City, Utah, USA, 2013. p 3370.

19. Dimitrov I, Douglas D, Ren J, Smith NB, Webb AG, Sherry AD, Malloy C. In vivo determination of human breast fat composition by 1H magnetic resonance spectroscopy at 7T. Magnetic Resonance in Medicine 2012;67(1):20-26.

20. van de Bank BL, Voogt IJ, Italiaander M, Stehouwer BL, Boer VO, Luijten PR, Klomp DWJ. Ultra high spatial and temporal resolution breast imaging at 7T. NMR in Biomedicine 2012.

21. Italiaander M, Voogt IJ, van Kalleveen I, Stehouwer BL, van der Velde T, Luijten PR, Boer VO, Klomp DJ. Uniform bilateral breast MRI at 7T with dual transmit and 30-channel receive. In: Proceedings of the 21st Annual Meeting of ISMRM. Salt Lake City, Utah, USA, 2013. p 2729.

22. Kim J, Zhao Y, Krishnamurthy N, Zhao T, Bae KT, Ibrahim TS. High temporal and spatial resolution breast MR imaging at 7T; Feasibility Study using 8-to-1 channel Tx-only Array Combined with 8 channel Rx-only Insert. In: Proceedings of the 21st Annual Meeting of ISMRM. Salt Lake City, Utah, USA, 2013. p 4396.

23. Orzada S, Maderwald S, Kopp L, Ladd ME, Nassenstein K, Bitz AK. A 16-channel micro strip Tx/Rx array for bilateral breast imaging at 7 tesla. In: Proceedings of the 20th Annual Meeting of ISMRM. Melbourne, Australia, 2012. p 430.

24. Lee RF, Moy L, Brown R, McGorty K, Stefanescu C, Wang Y, Peck N. 7T high resolution breast MRI. In: Proceedings of the 14th Annual Meeting of ISMRM. Seattle, Washington, USA, 2006. p 2900.

25. Webb AG, Collins CM. Parallel transmit and receive technology in high-field magnetic resonance neuroimaging. International Journal of Imaging Systems and Technology 2010;20(1):2-13.

26. Collins CM, Smith MB. Calculations of B1 distribution, SNR, and SAR for a surface coil adjacent to an anatomically-accurate human body model. Magnetic Resonance in Medicine 2001;45:692-699.

27. Roemer P, Edelstein W, Hayes C, Souza S, Mueller O. The NMR phased array. Magnetic Resonance in Medicine 1990;16(2):192-225.

28. Weiger M, Pruessmann KP, Leussler C, Roschmann P, Boesiger P. Specific coil design for SENSE- a six-element cardiac array. Magnetic Resonance in Medicine 2001;45:495-504.

29. Bloch F, Hansen WW, Packard ME. Nuclear induction. Physical Review 1946;69:127.

30. Purcell EM, Torrey HC, Pound RV. Resonance absorption by nuclear magnetic moments in a solid. Physical Review 1946;69:37.

31. Lauterbur PC. Image formation by induced local interactions: Examples employing nuclear magnetic resonance. Nature 1973;242:190-191.

32. Mansfield P. Multi-planar image-formation using NMR spin echos. Journal of Physics C-Solid State Physics 1977;10:L55-L58.

33. Wright SM. ELEN 648: Principles of MRI. College Station: Course Notes copyright Steven M. Wright, Texas A&M University; 2007.

34. Hu X, Norris DG. Advances in high-field magnetic resonance imaging. Annual Review of Biomedical Engineering 2004;6:157-184.

35. Lupo JM, Li Y, Hess CP, Nelson SJ. Advances in ultra-high field MRI for the clinical management of patients with brain tumors. Current Opinion in Neurology 2011;24:605-615.

36. Choi C, Dimitrov I, Douglas D, Zhao C, Hawesa H, Ghose S, Tamminga CA. In vivo detection of serine in the human brain by proton magnetic resonance spectroscopy (1H-RS) at 7 Tesla. Magnetic Resonance in Medicine 2009;62(4):1042-1046.

37. Atkinson IC, Thulborn KR. Feasibility of mapping the tissue mass corrected bioscale of cerebral metabolic rate of oxygen consumption using 17-oxygen and 23-sodium MR imaging in a human brain at 9.4 T. NeuroImage 2010;51(2):723-733.

38. Fleysher L, Oesingmann N, Stoeckel B, Grossman RI, Inglese M. Sodium long-component T2* mapping in human brain at 7 tesla. Magnetic Resonance in Medicine 2009;62(5):1338-1341.

39. Qiao H, Zhang X, Zhu XH, Du F, Chen W. In vivo 31P MRS of human brain at high/ ultrahigh fields: A quantitative comparison of NMR detection sensitivity and spectral resolution between 4 T and 7 T. Magnetic Resonance Imaging 2006;24(10):1281-1286.

40. Ladd ME. High-field-strength magnetic resonance: Potential and limits. Top Magnetic Resonance Imaging 2007;18(2):139-152.

41. Rooney WD, Johnson G, Li X, Cohen ER, Kim SG, Ugurbil K, Springer CS. Magnetic field and tissue dependencies of human brain longitudinal 1H20 relaxation in vivo. Magnetic Resonance in Medicine 2007;57(2):308-318.

42. De Martino F, Schmitter S, Moerel M, Tian J, Ugurbil K, Formisano E, Yacoub E, Van de Moortele P. Spin echo functional MRI in bilateral auditory cortices at 7 T: An application of B1 shimming. NeuroImage 2012;63:1313-1320.

43. Frischer J, God S, Gruber A, Saringer W, Grabner G, Gatterbauer B, Kitz K, Holzer S, Kronnerwetter C, Hainfellner J. Susceptibility-weighted imaging at 7 T: Improved diagnosis of cerebral cavernous malformations and associated developmental venous anomalies. NeuroImage: Clinical 2012;1:116-120.

44. Pruessmann KP, Weiger M, Scheidegger M, Boesiger P. SENSE: Sensitivity encoding for fast MRI. Magnetic Resonance in Medicine 1999;42:952-962.

45. Robson PM, Grant AK, Madhuranthakam AJ, Lattanzi R, Sodickson D, McKenzie CA. Comprehensive quantification of signal-to-noise ratio and g-factor for image-based and k-space-based parallel imaging reconstructions. Magnetic Resonance in Medicine 2008;60:895-907.

46. Carlson JW. An algorithm for NMR imaging reconstruction based on multiple RF receiver coils. Journal of Magnetic Resonance 1987;74(2):376-380.

47. Hutchinson M, Raff U. Fast MRI data acquisition using multiple detectors Magnetic Resonance in Medicine 1988;6:87-91.

48. Kelton JR, Magin RL, Wright SM. An algorithm for rapid image acquisition using multiple receiver coils. In: Proceedings of the 8th Annual Meeting of the SMRM, Amsterdam, NE, 1989. p 1172.

49. Ra JB, Rim CY. Fast imaging using subencoding data sets from multiple detectors. Magnetic Resonance in Medicine 1993;30:142-145.

50. Sodickson D, Manning WJ. Simultaneous acquisition of spatial harmonics (SMASH): Fast imaging with radiofrequency coil arrays. Magnetic Resonance in Medicine 1997;38:591-603.

51. Griswold MA, Jakob PM, Nittka M, Goldfarb JW, Haase A. Partially parallel imaging with localized sensitivities (PILS). Magnetic Resonance in Medicine 2000;44:602-609.

52. Kyriakos WE, Panych LP, Kacher DF, Westin C, Bao SM, Mulkern RV, Jolsez FA. Sensitivity profiles from an array of coils for encoding and reconstruction in parallel (SPACE RIP). Magnetic Resonance in Medicine 2000;44:301-308.

53. Griswold MA, Jakob PM, Heidemann RM, Nittka M, Jellus V, Wang J, Kiefer B, Haase A. Generalized autocalibrating partially parallel acquisitions (GRAPPA). Magnetic Resonance in Medicine 2002;47:1202-1210.

54. Griswold MA. Basic Reconstruction Algorithms for Parallel Imaging. In: Baert AL, Knauth M, Sartor K, editors. Parallel Imaging in Clinical MR applications. Berlin: Springer; 2007. p 19-36.

55. Sodickson D. Spatial Encoding Using Multiple RF Coils: SMASH Imaging and Parallel MRI. Encyclopedia of Magnetic Resonance. New York: John Wiley & Sons, Ltd. ; 2007.

56. Kuhl CK, Jost P, Morakkabati N, Zivanovic O, Schild HH, Gieseke J. Contrast-enhanced MR imaging of the breast at 3.0 and 1.5 T in the same patients: Initial experience. Radiology 2006;239(3):666-676.

57. Nnewihe AN, Grafendorfer T, Daniel BL, Calderon P, Alley MT, Robb F, Hargreaves BA. Custom-fitted 16-channel bilateral breast coil for bidirectional parallel imaging. Magnetic Resonance in Medicine 2011;66(1):281-289.

58. Marshall H, Devine PM, Shanmugaratnam N, Fobel R, Siegler P, Piron CA, Plewes DB. Evaluation of multicoil breast arrays for parallel imaging. Journal of Magnetic Resonance Imaging 2010;31(2):328-338.

59. Zhu J, Kurihara Y, Kanemaki Y, Ogata H, Fukuda M, Nakajima Y, Maeda I. Diagnostic accuracy of high-resolution MRI using a microscopy coil for patients with presumed DCIS following mammography screening. Journal of Magnetic Resonance Imaging 2007;25(1):96-103.

60. Brown R, Storey P, Geppert C, McGorty K, Leite A, Babb J, Sodickson D, Wiggins GC, Moy L. Breast MRI at 7 tesla with a bilateral coil and robust fat suppression. Journal of Magnetic Resonance Imaging 2013. doi: 10.1002/jmri.24205

61. McDougall MP, Cheshkov S, Rispoli JV, Malloy C, Dimitrov I, Wright SM. Quadrature transmit coil for breast imaging at 7T using forced current excitation for improved homogeneity. Journal of Magnetic Resonance Imaging 2014. doi: 10.1002/jmri.24473

62. Rispoli JV, Cheshkov S, Dimitrov I, Malloy C, Wright SM, McDougall MP. A quadrature volume transmit coil for breast imaging and spectroscopy at 7 tesla. In: Proceedings of the 20th Annual Meeting of the ISMRM, Melbourne, Australia, 2012. p 2635.

63. Umutlu L, Maderwald S, Kraff O, Theysohn JM, Kuemmel S, Hauth EA, Forsting M, Antoch G, Ladd ME, Quick HH. Dynamic contrast-enhanced breast MRI at 7 tesla utilizing a single-loop coil: A feasibility trial. Academic Radiology 2010;17(8):1050-1056.

64. Li B, Wang H, Weber E, Li Y, Trakic A, Lee DJ, Farhat S, Glover P, Bowtell R, Crozier S. A 7T "capless" transceive breast coil. In: Proceedings of the 18th Annual Meeting of the ISMRM, Stockholm, Sweden, 2010. p 3816.

65. Warmington LL, Adriany G, Snyder C, Auerbach EJ, Bolan PJ. 7T breast imaging with a 2-channel bilateral loop design. In: Proceedings of the 17th Annual Meeting of the ISMRM, Honolulu, Hawaii, USA, 2009. p 3006.

66. Cui J, Dimitrov I, Cheshkov S, McDougall MP, Malloy C, Wright SM. Switchable bilateral/unilateral 7T breast coil using forced current excitation. In: Proceedings of the 21st Annual Meeting of the ISMRM, Salt Lake City, Utah, USA, 2013. p 2727.

67. Zheng T, Yang X, Finnerty M, Heilman J, Herczak J, Fujita H, Wiggins GC, Brown R, Stoeckel B. A 7-tesla high density Tx/Rx mammography coil. In: Proceedings of the 19th Annual Meeting of the ISMRM, Montréal, Canada, 2011. p 3819.

68. Wiggins G, Triantafyllou C, Potthast A, Reykowski A, Nittka M, Wald L. 32-channel 3 tesla receive-only phased-array head coil with soccer-ball element geometry. Magnetic Resonance in Medicine 2006;56(1):216-223.

69. Wiggins GC, Polimeni JR, Potthast A, Schmitt M, Alagappan V, Wald LL. 96-Channel receive-only head coil for 3 tesla: Design optimization and evaluation. Magnetic Resonance in Medicine 2009;62(3):754-762.

70. Keil B, Alagappan V, Mareyam A, McNab JA, Fujimoto K, Tountcheva V, Triantafyllou C, Dilks DD, Kanwisher N, Lin W, Grant PE, Wald LL. Size-optimized 32-channel brain arrays for 3T pediatric imaging. Magnetic Resonance in Medicine 2011;66:1777-1787.

71. Wiggins GC. Receive arrays. In: Proceedings of the 20th Annual Meeting of the ISMRM, Melbourne, Australia, 2012. Educational Session Oral Talk.

72. Sodickson D, Ohliger M, Lattanzi R, Wiggins GC. Coil Array Design for Parallel Imaging: Theory and Applications. Encyclopedia of Magnetic Resonance. New York: John Wiley & Sons, Ltd. ; 2007.

73. High Power PIN Diodes: MA4P HIPAX Series. M/A-COM, Inc. www.macomtech.com.

74. Doty F, Connick TJ, Ni XZ, Clingan MN. Noise in high-power, high frequency double-tuned probes. Journal of Magnetic Resonance 1988;77:536-549.

75. Bolan PJ, Garwood M, Rosen MA, Levering A, Blume JD, Esserman LJ, Hylton N. Design of quality control measures for a multi-site clinical trial of breast MRS - ACRIN 6657. In: Proceedings of the 16th Annual Meeting of the ISMRM, Toronto, Canada, 2008. p 1588.

76. Brown R, Wang Y, Spincemaille P, Lee RF. On the noise correlation matrix for multiple radio frequency coils. Magnetic Resonance in Medicine 2007;58(2):218-224.

77. Wright SM, Wald LL. Theory and application of array coils in MR spectroscopy. NMR in Biomedicine 1997;10:394-410.

78. Wright SM. Receiver Loop Arrays. Encyclopedia of Magnetic Resonance. New York: John Wiley & Sons, Ltd.; 2011.

79. Kellman P, McVeigh ER. Image reconstruction in SNR units: A general method for SNR measurement. Magnetic Resonance in Medicine 2005;54(6):1439-1447.

80. Wiesinger F, Van de Moortele P, Adriany G, De Zanche N, Ugurbil K, Pruessmann KP. Parallel imaging performance as a function of field strength-an experimental investigation using electrodynamic scaling. Magnetic Resonance in Medicine 2004;52:953-964.

81. Larkman DJ. The g-Factor and Coil Design. In: Baert AL, Brady LW, Heilmann HP, Knauth M, Molls M, Sartor K, editors. Parallel Imaging in Clinical MR Applications. Germany: Springer; 2007.

82. Sodickson D, Hardy CJ, Zhu Y, Giaquinto RO, Gross P, Kenwood G, Niendorf T, Lejay H, McKenzie CA, Ohliger M, Grant AK, Rofksy NM. Rapid volumetric MRI using parallel imaging with order-of-magnitude accelerations and a 32-element RF coil array: Feasibility and implications. Academic Radiology 2005;12(5):626-635.

83. Larkman DJ, Nunes RG. Parallel magnetic resonance imaging. Physics in Medicine and Biology 2007;52:R15-R55.

84. U.S. Food and Drug Administration. Guidance for industry: Guidance for the submission of premarket notifications for magnetic resonance diagnostic

devices.http://www.fda.gov/MedicalDevices/DeviceRegulationandGuidance/GuidanceDocuments/ucm073817.htm; 1998.

85. Lanz T, Griswold MA. Concentrically shielded surface coils - a new method for decoupling phased array elements. Proceedings of the 14th Annual Meeting of the ISMRM, Seattle, WA, USA, 2006. p 217.

86. Gilbert KM, Curtis AT, Gati JS, Klassen LM, Villemaire LE, Menon RS. Transmit/receive radiofrequency coil with individually shielded elements. Magnetic Resonance in Medicine 2010;64(6):1640-1651.

87. McDougall MP, Wright SM, Rispoli JV, Carillo M, Dimitrov I, Cheshkov S, Malloy C. A printed loop element with integrated capacitors and co-planar shield for 7 tesla. In: Proceedings of the 19th Annual Meeting of the ISMRM, Montréal, Canada, 2011. p 1875.

88. By S, Rispoli JV, Dimitrov I, Cheshkov S, Malloy C, Wright SM, McDougall MP. Effects of co-planar element shielding on array performance at 7T. In: Proceedings of the 21st Annual Meeting of the ISMRM, Milan, Italy, 2014. (Accepted)

89. Cheshkov, S., G. Gilbert, I. Dimitrov, S. By, J. V. Rispoli, M. P. McDougall, S. M. Wright, S. Seiler and C. Malloy. In-vivo breast microcalcification detection via susceptibility weighted imaging at 7T. In: Proceedings of the 21st Annual Meeting of the ISMRM, Milan, Italy, 2014. (Accepted)